# 2

# Surface geophysical methods

**J.-L. Mari and G. Paixach**

Historically, geophysical methods have played a pivotal role in the exploration of oil, gas, and minerals, serving as the backbone of resource discovery for decades. However, the landscape of geophysical applications is evolving to meet the demands of emerging domains holding significant economic, technological, social, and environmental importance. One such domain is geothermal energy, which is becoming a potential candidate in the global push toward heat and electricity decarbonization.

The shift towards geothermal energy requires a deeper understanding of the subsurface, not only in sedimentary basins but also in areas characterized by igneous formations. Effective site investigation for geothermal projects needs characterization of the subsurface through different geophysical methods.

There are various geophysical methods, each based on distinct theoretical principles, that provide valuable data about subsurface materials. By acquiring and analyzing this data through specific geophysical surveys, we can better understand the subsurface properties and characteristics, offering important insights for exploring and managing subsurface resources and developing geotechnical engineering.

Geophysical methods encompass various techniques, each designed to characterize specific properties of geological formations and rocks. Among the most widely used methods are seismic, magnetic, electrical, electromagnetic, and gravity surveys.


DOI: https://doi.org/10.1051/978-2-7598-3752-6.c002

Each method provides unique and complementary information about the subsurface, highlighting the importance of using multiple geophysical techniques in geothermal exploration. Integrating results from these diverse geophysical methods is crucial for creating a comprehensive image of the subsurface, which is essential for successful geothermal exploration, production, and monitoring.

By combining seismic data with electrical resistivity, for example, geoscientists can correlate structural information with fluid content, improving the accuracy of reservoir models. Similarly, integrating magnetic and gravity data can enhance the understanding of the geological context, such as the presence of igneous intrusions or fault systems, which are critical for assessing geothermal potential. This multidisciplinary approach not only enhances the precision of subsurface imaging but also reduces the uncertainty in locating and exploiting geothermal resources, ultimately contributing to more efficient and sustainable geothermal energy production.

Surface geophysical methods are usually non-invasive techniques used to investigate the properties of subsurface materials from the Earth's surface. Surface geophysical methods are relatively cost-effective and efficient, covering large areas quickly without drilling. They provide broad, low to medium-resolution data making them ideal for exploration and mapping.

However processing and interpreting surface geophysical survey data usually requires prior knowledge of the subsurface geological structure, typically obtained from preliminary reconnaissance geological field studies, borehole data, and rock physics modeling.

- Reconnaissance geological field studies involve visual inspections and preliminary assessments of geological formations, using either on-foot surveys or satellite imagery. Detailed mapping and rock sampling are subsequently conducted to gain a more precise understanding of the surface geology, typically onshore.
- Borehole data are collected by placing sensors inside drilled wells to measure subsurface properties at specific depths. This method provides high-resolution, localized information on properties like lithology, porosity, and fluid content. Borehole data acquisition is generally expensive due to the need for drilling, logging equipment, and operational time to drill and instrument the borehole.
- Rock physics modeling is fundamental to interpreting and processing the results of geophysical surveys because it bridges the gap between raw geophysical data and the underlying geological realities. It provides the essential framework for understanding how different rock types, with their unique mineral compositions, porosities, and fluid contents, respond to various geophysical methods such as seismic, electrical, and magnetic surveys.

The best strategy for selecting and combining different geophysical methods hinges on balancing the four key factors that govern their effectiveness:

- penetration depth,
- vertical and lateral resolutions,
- signal-to-noise ratio,
- and contrast in physical properties.

First, penetration depth is crucial for determining how deeply a method can probe the subsurface. Methods like seismic surveys offer deep penetration in general, making them ideal for exploring deeper geothermal reservoirs, while methods like electrical resistivity are best suited for shallower investigations. Therefore, selecting a method with appropriate penetration depth ensures that the target depth of interest is adequately covered. The concept of penetration depth in geophysical methods is controlled by several factors, which vary depending on the specific technique used. These factors include the type of energy source (such as seismic waves, electrical currents, or electromagnetic fields), the frequency or wavelength of the signal, the physical properties of the subsurface materials, and environmental conditions. A key factor controlling penetration depth is the frequency or wavelength of the signal. In general, lower-frequency signals penetrate deeper into the Earth, but with lower resolution, while higher-frequency signals provide more detailed images but with shallower penetration. The composition and physical properties of the subsurface materials also play a significant role in determining penetration depth. The strength or intensity of the energy source also affects how deep a geophysical signal can penetrate. In seismic methods, for example, a stronger source (such as a large explosion) will generate seismic waves capable of traveling deeper into the subsurface compared to a weaker source (like a small hammer strike).

Second, vertical and lateral resolutions are essential for accurately imaging subsurface features. The vertical and lateral resolutions of geophysical methods – the ability to distinguish between subsurface features at different depths (vertical resolution) and across horizontal distances (lateral resolution) – are influenced by several key factors. High-resolution methods, such as ground-penetrating radar (GPR) or high-frequency seismic surveys, are excellent for detailed imaging of shallow subsurface structures, whereas lower-resolution methods might be more suitable for broader, regional surveys. Combining methods with complementary resolutions helps build a detailed and comprehensive subsurface model. These include the frequency or wavelength of the signal, the spacing of data collection points (survey geometry), the physical properties of the subsurface, and the processing techniques used to refine the data. The wavelength of the signal used largely determines the vertical resolution of a geophysical method. In seismic surveys, for example, higher-frequency seismic waves can detect thin layers, whereas low-frequency waves may smooth over fine details but penetrate deeper. Lateral resolution is typically controlled by the density of data acquisition across the survey area. Closely spaced measurement points (e.g., seismic receiver stations, electrodes, or magnetometers) provide better lateral resolution, enabling the detection of smaller subsurface features. In contrast, widely spaced points result in a coarser lateral image, potentially missing finer details. In areas with complex geological structures or heterogeneous materials, lateral resolution can be reduced as the signal may be scattered or absorbed by irregularities in the subsurface. This is particularly relevant in seismic and electromagnetic methods, where subsurface heterogeneities can blur or obscure smaller features.

The signal-to-noise ratio is another critical factor. The concept of signal-to-noise ratio (SNR) is critical in geophysical methods as it measures the clarity and reliability of the data collected during a survey. In essence, SNR compares the strength of the desired

signal – representing the geophysical properties of the subsurface – to the background noise, which may originate from environmental, instrumental, or human-made sources. A high SNR indicates that the signal is clear and distinct from the noise, enabling a more accurate interpretation of subsurface features. A low SNR means the signal is masked by noise, making it difficult to extract useful information. Each geophysical method is affected by noise differently. For instance, seismic methods can be disrupted by surface vibrations from traffic or machinery, while electromagnetic methods are sensitive to electrical interference from power lines or other sources. Improving SNR is crucial for ensuring reliable geophysical survey results. Techniques like stacking, filtering, and signal processing are commonly used to enhance the signal and reduce noise across various methods. Seismic surveys, for example, often employ stacking, where multiple seismic traces are combined to amplify the signal and diminish random noise. In electrical and electromagnetic surveys, filtering techniques can be applied to isolate the frequencies of interest and suppress unwanted noise. The success of a geophysical method depends on achieving a balance between maximizing signal strength and minimizing noise, which varies depending on the survey environment and the specific method used.

In passive seismic methods, the concept of signal-to-noise ratio is redefined because what is traditionally considered "noise" becomes the primary source of useful data. Unlike active seismic surveys, which generate artificial seismic waves using controlled sources like explosions or vibrators, passive seismic techniques rely on naturally occurring or ambient seismic noise, such as microtremors, ocean waves, or human activities. This background noise, which would typically be seen as a nuisance in active seismic methods, is instead harnessed as the signal itself. Passive seismic methods, such as seismic interferometry or ambient noise tomography, process this ambient noise to extract valuable information about the Earth's subsurface. The challenge in passive seismic surveys is not eliminating noise but rather distinguishing between different types of noise to identify the most useful signals. For example, seismic interferometry uses cross-correlation techniques to turn ambient noise into coherent seismic waves, which can then be interpreted similarly to traditional seismic data. This approach is particularly valuable in environments where active seismic surveys are not feasible, such as urban areas or environmentally sensitive regions. It offers a cost-effective, non-invasive means of subsurface exploration, making it an important tool in geothermal energy exploration and monitoring.

Finally, the contrast in physical properties refers to how distinct the geological features are in terms of their physical characteristics. Geophysical methods are most effective when there is a significant contrast, such as differences in density or electrical conductivity, between target formations and surrounding materials. Therefore, choosing methods that can exploit these contrasts – like gravity surveys for density differences or electromagnetic methods for conductivity variations – optimizes the detection of specific subsurface features.

By carefully considering these factors, geoscientists can select and combine geophysical methods that complement each other, providing a more accurate and comprehensive understanding of the subsurface, which is crucial for effective geothermal exploration and other subsurface investigations.

Subsurface investigations inherently carry uncertainty, especially when working in complex or poorly understood geological environments. A feasibility study reduces this uncertainty by identifying the limitations and strengths of each method in the specific context of the site. This helps reduce the risk of failed surveys or inaccurate interpretations, which can lead to expensive rework or the failure of large-scale projects, such as geothermal energy exploration or construction planning. A feasibility study helps identify the most suitable methods based on the geological conditions of the site. For example, if there is little contrast in the seismic velocities of rock layers but a strong difference in electrical resistivity, electrical methods may be more effective than seismic methods. This preliminary evaluation ensures that only the most appropriate and effective methods are deployed in the main survey. Full-scale geophysical surveys can be costly, especially when multiple methods are involved. A feasibility study allows for testing the effectiveness of the methods on a smaller scale, reducing the risk of investing in techniques that may not produce useful results. Also, geophysicists can tailor their approach to mitigate potential problems, such as improving signal-to-noise ratios or adjusting survey geometry.

Before delving into the specifics of each geophysical method, it is essential to review the characteristics of rocks, including their mineral composition, porosity, and other physical properties. These characteristics significantly influence the outcomes of geophysical surveys. For instance, the mineral content of a rock determines its magnetic and electrical properties, while porosity affects its ability to store and transmit fluids, impacting seismic and resistivity measurements. Additionally, the overall rock properties, such as density and elasticity, play a crucial role in how seismic signals propagate.

A thorough review of these rock properties is necessary to accurately interpret geophysical data and effectively apply these methods in geothermal exploration and other subsurface investigations. Following a concise review of the physical and pore space properties of rocks, we provide an overview of surface geophysical methods and illustrate their application with selected field examples. Since different geophysical methods provide complementary information, integrating their results often provides the best subsurface model.

## 2.1 Physical properties of rocks and pore space properties

This discussion emphasizes the characterization of natural rocks, which are inherently heterogeneous and composed of diverse minerals with varying physical properties, shapes, sizes, and spatial arrangements. These complexities, along with boundary effects, interactions, and thermodynamic conditions, fundamentally influence the physical properties of rocks.

For a geophysicist, rock is composed of three elements: the matrix, the porosity, and the fluids.

The matrix is the solid part constituted of minerals, each of them characterized by their physical properties such as density, velocity, resistivity, susceptibility, etc.

Porosity refers to the amount of empty space within the rock, often described as the fraction of the rock's total volume that is occupied by voids, cracks, or pores. These pores can vary greatly in size, shape, and connectivity, and they significantly influence the rock's ability to store fluids. Porosity is expressed as a percentage, with higher values indicating more pore space. The arrangement and distribution of these pores within the matrix are crucial for determining other properties, such as permeability, which describes how easily fluids can move through the rock. Permeability seems to be the most important (and hard to determine) property for all reservoir problems. It controls whether the rock can deliver or transmit fluids or not.

The fluids are pore-filling materials: water, oil, gas, air, and pollutants, each of them having specific physical properties. These fluids, with their specific physical properties like viscosity and conductivity, play a major role in the rock's overall behavior.

The physical properties of these elements will condition the physical properties of the rock (Figure 2.1).

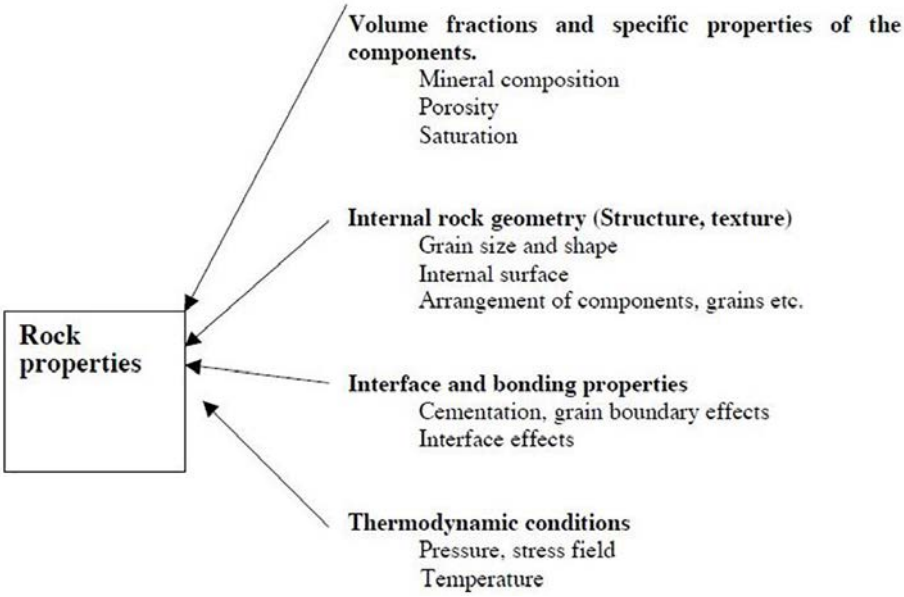


Figure 2.1 *Physical properties of rocks (after D. Chapellier, IFP School course, personal communication).*

**Rock physics modeling** is the process of quantitatively describing the relationship between the physical properties of rocks (such as porosity, mineral composition, and fluid saturation) and their geophysical properties (such as elastic wave velocities, and electrical conductivity). The ultimate objective is to interpret subsurface geology, reservoir characteristics, and fluid content from geophysical measurements.

Rock physics modeling can involve **theoretical models** based on physical laws combined with numerical simulations or **empirical relationships** derived from laboratory measurements or field data.

The estimation of physical parameters such as seismic velocities and attenuation or resistivity obtained by geophysical methods associated with experimental relationships established from laboratory experiments allows the estimate of porosity or permeability distributions in geological formations.

### 2.1.1 *Porosity*

Porosity $\Phi$ is defined as the ratio of the volume of pore space to the total or bulk volume of the rock. Porosity is expressed as a decimal fraction or a percentage (%). Porosity is the result of various geological, physical, and chemical processes, and is generated during the genesis of the rock as "primary porosity", and/or during the geological history of the rock as "secondary porosity" (tectonic processes (fractures), chemical processes, dissolution). Total porosity is the sum of the primary and the secondary porosity.

The main factors, which influence primary porosity, are:

- Grain and pore geometrical properties (arrangement and shape of the rock grains, grain size distribution),
- Diagenetic processes, amount of cement,
- Depth and pressure (which also influences secondary porosity)

Theoretically, porosity for given packing is independent of grain size. However, porosity shows a tendency to increase with the change from spherical or well-rounded grains to angular particles. Decrease of porosity primarily results from packing and cementation for sands and sandstone, and from compaction for clays and shale. This reflects a general tendency of decreasing porosity with increasing depth.

Effective porosity is the porosity that is available for free fluids; it excludes all non-connected porosity. Effective porosity could be much lower than the total porosity when the pores are not connected or when the pores are so small that fluids cannot circulate.

For a clean formation, if the matrix and fluid velocities are known, porosity can be computed from the acoustic $V_p$ velocities by using the formula given by Wyllie et al. (1956) expressed in velocities. It is given by the following equation:

$$\Phi = \left( \frac{v_{ma} - v_p}{v_{ma} - v_f} \right) \frac{v_f}{v_p} \tag{2.1}$$

with $V_{ma}$ the matrix velocity, $V_f$ the fluid velocity.

Porosity can also be estimated by electrical measurement. Archie (1942) has shown empirically that for water-saturated permeable formations, the relation between the true formation resistivity, $R_t$, and the resistivity, $R_w$, of the water impregnating the formation is given by:

$$\frac{R_t}{R_w} = F = \Phi^{-m} \tag{2.2}$$

where F is the "resistivity formation factor". $\Phi$ is proportional to the formation porosity and m is a "cementation factor", that is a formation characteristic. The F value derived from the resistivity measurement, $R_t$, is unaffected by the mineralogical constituents of the formation matrix. Although the "cementation factor" value may vary between 1.3 and 3 according to the formation lithology, an approximate value equal to 2 is generally adopted.

### 2.1.2 *Permeability*

Permeability describes the property of a porous rock regarding fluid flow through the pore space. It depends on the porosity, the pore space dimension, and geometry. In hydrogeology, the hydraulic permeability $K_f$ has the dimension of a velocity (mostly given in cm/s) (Figure 2.2). In practice, the unit DARCY (d) is commonly used. 1 Darcy is the permeability of a material that permits a volume flow of 1 $cm^3/s$ through a section of 1 $cm^2$ under a pressure gradient of 1 atm/cm of a fluid with a viscosity of 1 centipoise. One millidarcy, 1 md = $10^{-6}$cm/s.

Permeability depends in a very complex way on the properties of the pore space. The dominant influences are:

- Porosity: Permeability increases with increasing porosity, but this is strongly influenced by the rock type.
- Pore size: Permeability increases with increasing grain size; this is the dominant parameter, especially for sedimentary rocks.
- Pore shape and specific surface: Pore space geometry determines permeability and the capillary forces; these forces control the retention of water in the angles and capillaries between the grains.
- Arrangement of pores
- Permeability decreases with compaction and cementation.

Morlier and Sarda (1971) have looked at ultra-sonic data (P-wave and S-wave velocities, frequencies, and attenuations) and petrophysical data (porosity, permeability, specific surface) of numerous core plugs of different rock types (sandstone, limestone, carbonate). Their laboratory experiments have led them to the following results:

- When there is only one saturating fluid, the attenuation is an increasing function of frequency f and of the reverse of the kinematic viscosity ($\rho_f/\mu$ with $\rho_f$: fluid density, $\mu$: fluid viscosity (centipoise)).

- The attenuation δ depends on the structure of the rock (i.e. pore geometry).
- The attenuation δ can be expressed in terms of three structural parameters: porosity, permeability, and specific surface.

A law which fits their experimental results has been established:

$$\delta = \frac{CS}{\varphi}\left(\frac{2\pi k f \rho_f}{\mu}\right)^{1/3} \tag{2.3}$$

with:
δ: attenuation (dB/cm), f: frequency (Hz), ρf: fluid density, μ: fluid viscosity (centipoise), φ: porosity, S: Specific surface ($cm^2/cm^3$), C: calibration coefficient, k: permeability (mD, 1 mD = $10^{-15}$ $m^2$).

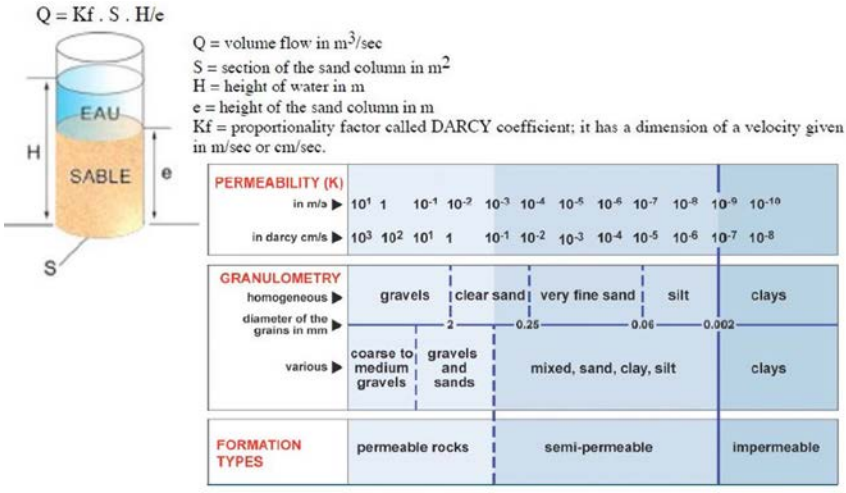


Figure 2.2 *Permeability Kf versus granulometry and formation types. After Dominique Chapellier (2001a).*

Figure 2.3 is an example of laboratory measurements on sandstone core plugs. The upper part of the figure shows the results obtained on cores with a constant specific surface, the lower part on cores with a variable specific surface, the specific surface being estimated based on the average pore radius measurement.

From equation (2.3), Mari et al. (2012) derived an indicator of permeability Ik-Seis, useable with seismic or acoustic data

$$\text{Ik-Seis} = \frac{(\varphi\delta / S)^3}{f} = \frac{(\varphi / SQ)^3}{f} \tag{2.4}$$

with
f: P-wave frequency, Q: quality factor, δ: attenuation, S: specific surface, φ: porosity.

It is necessary for computing the permeability from equations (2.3) or (2.4) to measure the attenuation of the formation and to calculate the effective specific surface of the formation.

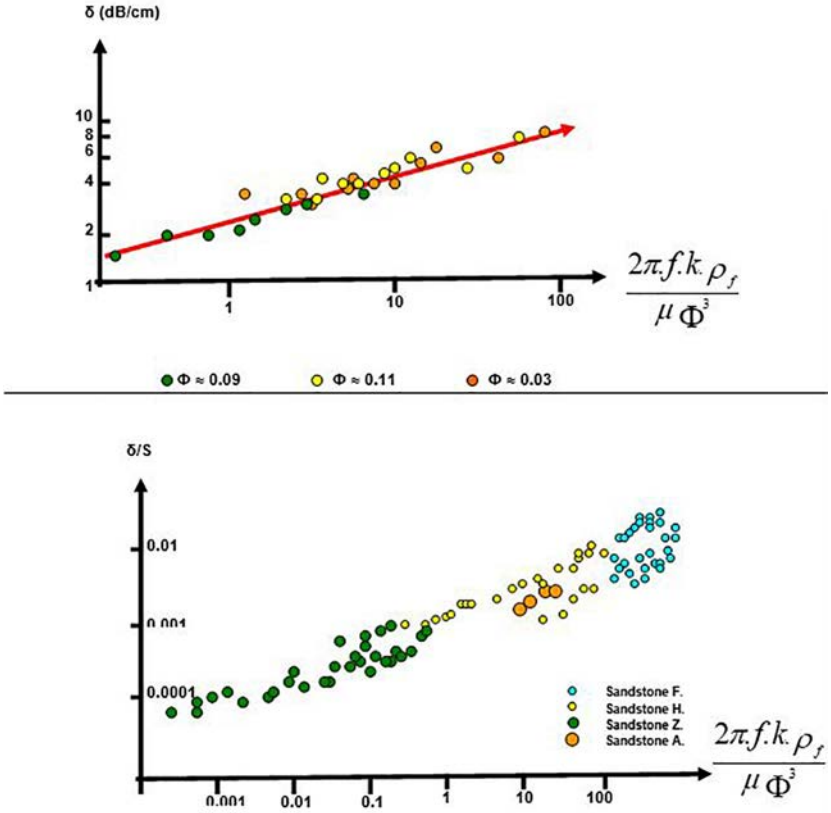


Figure 2.3 *Relationship between attenuation and petrophysical parameters (after Morlier and Sarda, 1971). Top: laboratory measurements on cores with constant specific surface. Bottom: laboratory measurements on cores with variable specific surface*

Theoretically, the effective specific surface S can be calculated from the porosity φ and the Klinkenberg permeability k (given in $m^2$ in equation (2.5) but typically reported in mD) using Kozeny's equation (Kozeny, 1927)

$$k = C_k(\varphi^3/S^2) \tag{2.5}$$

$$S_g = S/(1 - \varphi) \tag{2.6}$$

with φ: porosity, S: Specific surface, $S_g$: Specific surface with respect to grain volume, $C_k$: Kozeny's factor

The Kozeny's factor can be calculated from the porosity via a simple model of linear 3D interpenetrating tubes (Mortensen et al., 1998). The specific surface $S_g$ with respect to the bulk volume is given in 1/m in equations (2.5) and (2.6) but typically reported in $m^2/cm^3$. Fabricius et al. (2007) have found that the specific surface with

respect to grain volume ($S_g$) apparently does not depend on porosity. To remove the porosity effect on $V_p/V_s$ and mimic a reflected φ vs. log($S_g$) trend, they propose to use the following relationship between porosity φ, $V_p/V_s$ and $S_g$:

$$\log(S_g\, m) = a\varphi + b(V_p/V_s) + c \qquad (2.7)$$

where it should be observed that $S_g$ is multiplied by m to make $S_g$ dimensionless.

To establish equation (2.7), Fabricius et al. (2007) have looked at ultra-sonic data, porosity, and the permeability of 114 carbonate core plugs.

## 2.2 Geophysical methods

Geophysical methods are currently used to build 2D or 3D models of the sub-surface associated with variations of physical properties of rocks:

- Gravity method with density variations,
- Magnetic method with rock magnetization properties (magnetic susceptibility κ and remanence),
- Low frequency Electrical and EM methods with resistivity variations,
- High-frequency EM methods with permittivity variations (GPR),
- Seismic methods with velocity and density variations.

Figure 2.4 gives links between rocks and petrophysical parameters.

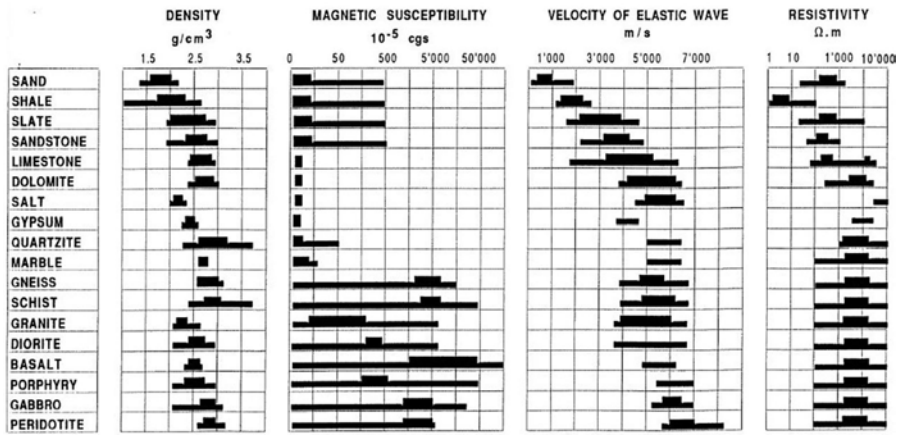


Figure 2.4 *Rocks and petrophysical parameters (density, magnetic susceptibility, velocity of elastic P-wave, resistivity) (after D. Chapellier, IFP School course, personal communication).*

The acquisition parameters must be selected to reach the depth of the target. The vertical and horizontal resolutions must be evaluated to know if the chosen method is well adapted to the sizes of the expected anomalies. Several methods can be combined as indicated in Figure 2.5, depending on the objective: Geological, Resources, Engineering.

| Problem | | Example | Methods and remarks |
|---|---|---|---|
| **Geological** | **Stratigraphical** | Sediments over Bedrock | Seismic refraction<br>Resistivity<br>seismic reflection |
| | **Erosional** | Buried channel | Seismic refraction, gravity, electromagnetic and resistivity |
| | | Buried Karstic surface | Electromagnetic and resistivity Radar<br>Seismic reflection |
| | **Structural** | Faults and fractures zones | Resistivity and EM<br>Seismic refraction and reflection<br>Magnetic and gravity |
| **Resources** | **Hydrocarbons** | Location of reservoir | Seismic reflection<br>Gravity and Magnetic<br>Borehole geophysics |
| | **Water** | Location of aquifer | Resistivity, EM, seismic refraction and reflection<br>Gravity and magnetic |
| | **Sand and gravel** | Gravel banks | Resistivity, EM<br>Gravity and magnetic<br>Marine: continuous seismic profiling |
| | **Clay** | Clay pockets | Resistivity and EM<br>P.P. |
| **Engineering** | **Elasticity modulus, density and porosity** | Dynamic deformation modulus | Seismic surface waves<br>Borehole seismic and density and porosity logs |
| | **Rock rippability** | Choice of excavation method | Seismic refraction |
| | **Corrosivity of soils** | Pipeline surveys | Resistivity |

Figure 2.5 *Geophysical methods versus objectives: Geological, Resources, Engineering (after D. Chapellier, IFP School course, personal communication).*

## 2.2.1 *Gravity method*

Gravity method concerns the study of the gravity field. The variations in gravity over the earth's surface have become a powerful technique in the investigation of geological structures at various depths. The variations in gravity reflect the inhomogeneous distribution of the densities in the ground. The density of the rocks (Figure 2.6) depends mainly on the rock composition and its porosity.

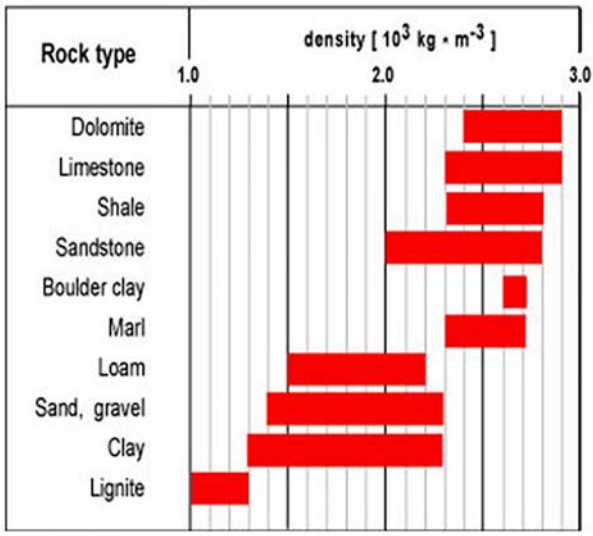


Figure 2.6 *Density versus rock type. After D. Chapellier (2001a).*

The purpose of a relative gravity survey is to directly map the structure of the subsurface. Gravity is the attractive force between two or more bodies of mass. The force, given by Newton's law, is proportional to the mass m of the object and decreases with distance R:

$$F = G\,M\,m/R^2 \tag{2.8}$$

$G = 6.674\times10^{-11}$ N·m$^2$·kg$^2$ is the universal gravitational constant, R = 6371 km radius of the earth, $M_{earth} = 5977\times10^{24}$ kg.

The force exerted on a body at the earth's surface is due to the attraction of the earth. The gravitational acceleration g (referred as gravity) may be considered as the force exerted by the earth on a unit mass: g = F/m.

The SI unit for the gravity, g, is m/s$^2$. In geophysics this unit is referred to as the Gal (in honor of Galileo). One-tenth of a miligal is called a gravity unit (g.u.), which is used more commonly in exploration work. 1 g.u. = 0.1 mGal.

The density contrast leads to a different gravitational force which is measured, and usually presented in mgal or $10^{-3}$ cm/s$^2$. To obtain information about the subsurface density from the gravity measurement, it is necessary to make several corrections to the measured value. The final corrected values of the gravity anomaly, is called Bouguer anomaly and is given by:

$$\Delta g = g_{obs} - g\varphi + \Delta g_{al} - \Delta g_{Boug} + TC \tag{2.9}$$

where $g_{obs}$ are gravity readings observed at each gravity station after corrections have been applied for instrument drift and earth tides. $g\varphi$ is the gravity at latitude $\varphi$. $\Delta g_{al} = 0.3086h$ is the Free air correction or elevation correction to consider the variation of elevation h between the measurement locations (a vertical decrease of gravity is associated with an increase of elevation). $\Delta g_{Boug} = 0.042\rho h$ is the correction from the excess mass material between the station and sea level. (variation of elevation h, density $\rho$). TC is the terrain correction that accounts for the presence of mass (for example hill) in the vicinity of the measurement station.

Bouguer anomalies are differences between actual gravity values and what would be expected from a uniform earth, which has the same latitude, elevation, and terrain. Gravity interpretation frequently begins with some procedure that separates the anomalies of interest from the smooth presumably deep regional effects. The regional effect could be obtained by a filtering process, such as upward continuation intended to emphasize or enhance the long wavelength components. The regional is subtracted from the observed gravity map or profile, and the resulting residual contains the component of the field which are caused by mass representing geological disturbances of interest.

Figure 2.7 is an example of Bouguer anomaly observed in Martinique (Girard, 2017). The studied area is located close to the site called "Anses d'Arlets", south-West of Martinique (Figure 2.7a). Geology is mainly composed of andesitic to dacitic products with basaltic lavas (age ranges from 1.5 to 0.35 million years). The density variation in the ground affects the gravity recorded in surface, and after some corrections have been applied, a Bouguer anomaly map can be obtained. The average density which decorrelates the more the topographic effect (Nettleton, 1939) is close to 2, and was used to compute the map shown in Figure 2.7b. A high pass filter was applied (cut length 8 km). Black dots are gravimetric measurements.

The U.S. Navy has developed a system to measure gravity gradients. In 1994, this technology began to be used in exploration (Bell et al., 1997). Normal gravity field $g_z$, also noted Gz, is the vertical pull of gravity at a location and is made up of two signals: one from the local geology and the other from the best-fitting ellipsoid field (Fairhead, 2015). In airborne gravity, the airborne gravimeter measures the sum ($g_z$ + a) of the vertical acceleration "a" and of the normal gravity field $g_z$. To recover the normal gravity field, the vertical acceleration must be canceled using additional information given by GPS measurements. The measurement of $g_z$ at two elevations $z + \Delta z/2$ and $z - \Delta z/2$ leads to the cancelation of the kinematic acceleration by computing the first vertical derivative Gzz of the gravity field. Such an approach is known as Gravity-gradiometry, the measurements being done by gravity gradiometers.

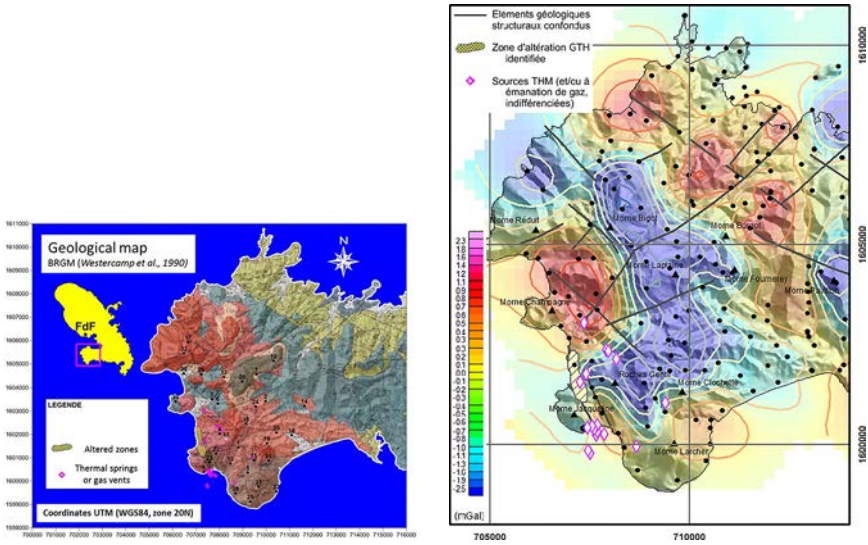


Figure 2.7 *Gravity method. Bouguer anomaly observed in Martinique (after Girard, 2017). Location map (a), Bouguer anomaly map (b)*

The gravitational field is composed of 3 vectors: the vertical vector component Gz, and two horizontal vector components Gx and Gy. The 3 vector components of gravity Gx, Gy and Gz have vertical and horizontal gradients: Gxx, Gxy, Gxz for Gx; Gyx, Gyy, Gyz for Gy; Gzx, Gzy and Gzz for Gz. The gradients are known as tensors. Because partial derivatives are independent of the order of differentiation, three of the tensors are identical to three other tensors (Gxy = Gyx, Gxz = Gzx, and Gyz = Gzy). Consequently, one only needs to measure five of the tensors to measure the Full Tensor Gradiometry (FTG) field (Figure 2.8a).

An 11×11 km Air-FTG™ survey with 100 m in-line, spacing (orientation NS) was flown over the Vinton, Salt Dome area onshore Louisiana, USA, in 2002 (Murphy and Mumaw, 2004). All five independent Tensor components were recorded and are shown in Figure 2.8b.

Gzz clearly maps the near-surface high-density caprock (outline shown in white). The other Tensor components reveal detailed information relating to the dominant geological structural control on the salt emplacement. Gxx and Gyy locate the NS and EW edges of the caprock feature and their negative sum yielding Gzz gives the expected positive Gzz anomaly. The variation in Gzz, Gxx and Gyy anomaly intensity indicate that the caprock itself is not of uniform shape. Gxz and Gyz locate the central axes of the salt feature, and with Gxx and Gyy help identify the dominant structural pattern. The salt appears to have been emplaced at the intersection of two dominant trends, i.e. NWSE and NESW. Gxy, showing the characteristic "2 positive 2 negative" anomaly pattern, helps constrain the geometric extent of the salt caprock.

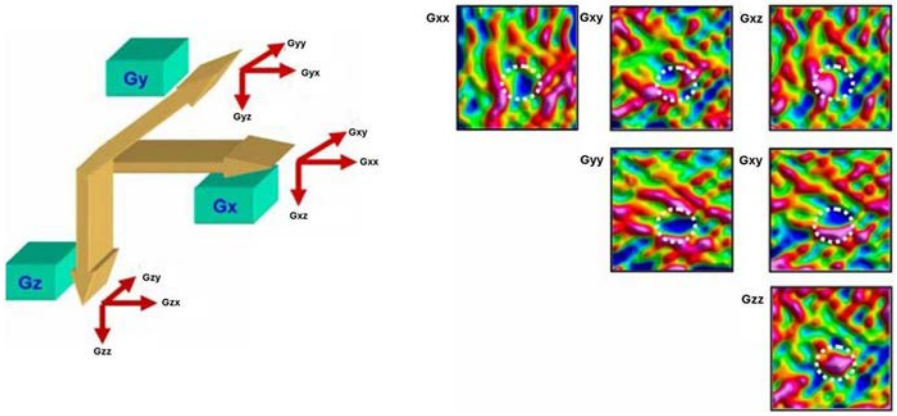


Figure 2.8 *Gravity Gradiometry method. (a) The full tensor gravitational field, (b) Tensor Display for the Vinton Dome Air-FTG™ survey. Gzz clearly images the cap rock on the salt dome (outline in white). The cap rock's response in each of the independent components is also circled (after Murphy and Mumaw, 2004).*

Time-lapse microgravity is used to identify the mass deficit that occurs in reservoirs in petroleum and geothermal fields because of mass extraction carried out during exploitation. The study, conducted by Pasaribu et al. (2024), explores the application of the time-lapse microgravity method at the Awibengkok geothermal field in Indonesia since the commencement of production. This method utilizes gravimeter equipment with a precision of up to 0.001 miligal (mgal) to monitor mass changes resulting from fluid extraction. Gravity measurements since 1994 reveal a significant annual average decrease in gravity acceleration (–9.2 microgals per year), indicating ongoing mass depletion in the reservoir. The approach includes digital leveling for gravity data correction and subsidence risk assessment. Gravity data modeling employs inversion methods to visualize density changes beneath the surface, demonstrating notable density decreases in production areas and localized increases near injection wells, suggesting potential dynamics of fluid recharge. Gravity changes that occurred from 1998 to 2008 and 1998 to 2017 are depicted in Figure 2.9. Decreasing gravity acceleration from1998 to 2010 was –230 µgal and increased in 2017 to over –500 µgal. The largest decrease in gravity acceleration occurs in the middle of proven area (blue to purple).

The gravity and gravity-gradiometry methods are particularly suitable for evaluating depth to basement and mapping basin 3D structures and basement features such as lineament, faults, etc.

For more information about the gravity method, we recommend reading the book written by Fairhead (2015).

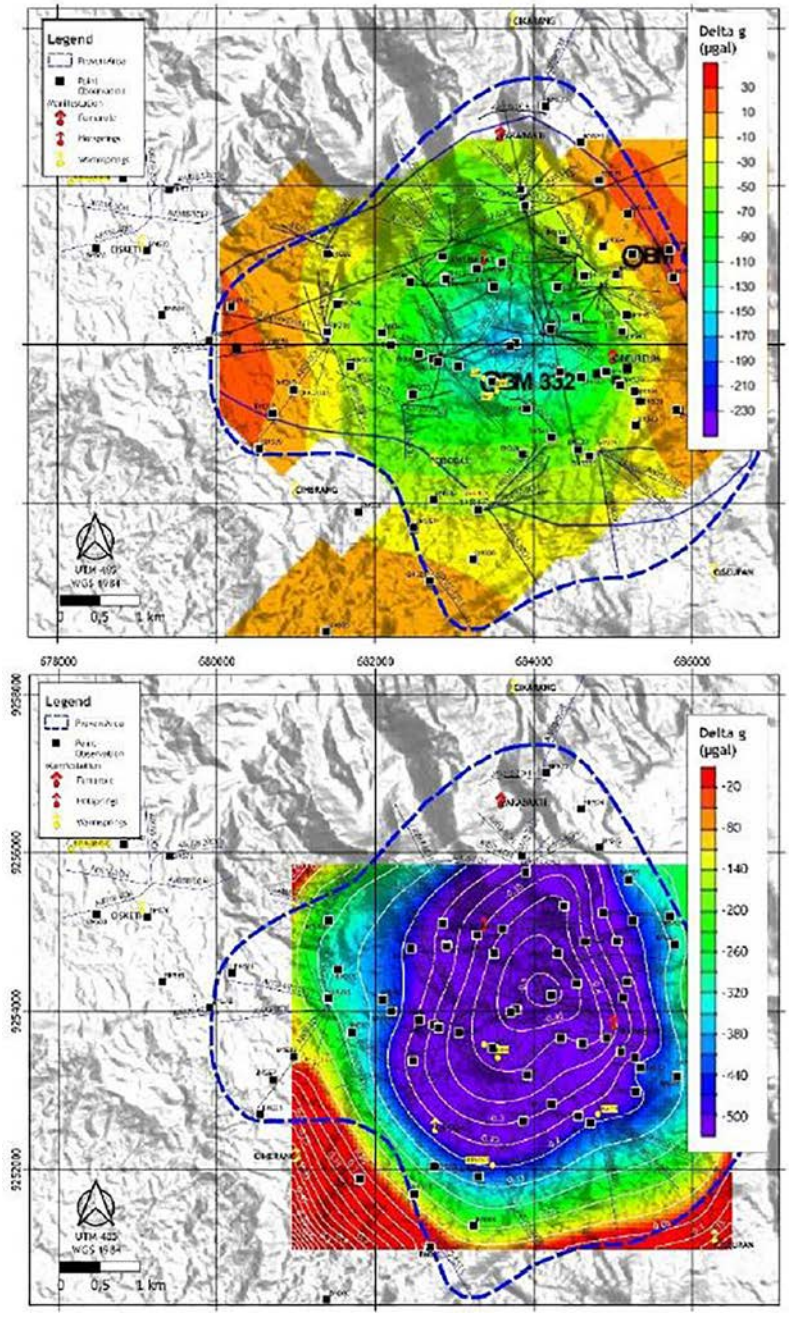


Figure 2.9 *Geothermal fluid production impact on density (after Pasaribu et al., 2024). Gravity changes map (on µgal) from 1998 to 2010 (top) and to 1998 to 2017 (bottom)*

## 2.2.2 *Magnetic method*

Magnetic properties describe the behavior of any substance under the influence of a magnetic field. All minerals are affected in some way by a magnetizing field. The capacity of a mineral to acquire magnetism by induction is described by its magnetic susceptibility. The strength of the induced magnetization M (magnetic dipole moment per unit volume) is directly related to the strength of the applied magnetic field H:

$$M = \kappa H \tag{2.10}$$

with $\kappa$ the magnetic susceptibility.

Rock types vary in magnetic susceptibility (Figure 2.10a). The most important fact in magnetic exploration for petroleum is that sedimentary rocks are nearly non-magnetic, that is; have very small susceptibility compared to basement rocks. The susceptibilities of non-sedimentary rock types are larger than those of sedimentary rocks by a factor of 10 to 1000 times. The magnetic fields measured in practice are flux densities. The unit is called Tesla T. For most geophysical purposes the tesla is too large as a unit and flux densities are more conveniently expressed in nanotesla (nT = $10^{-9}$ T).

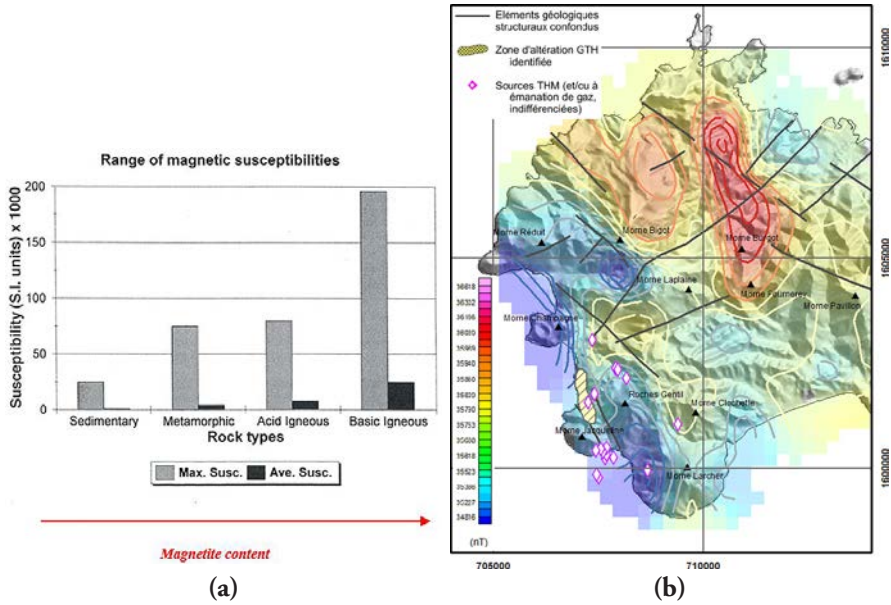


Figure 2.10 *Magnetic method. a: Magnetic susceptibility versus rock type (after D. Chapellier, IFP School course, personal communication), b: Magnetic anomaly observed in Martinique (after Girard, 2017).*

Magnetic exploration is primarily used in the first phases of geophysical work in the area. Magnetic surveying, performed with magnetometers (fluxgate magnetometer, proton-precession magnetometer...), is carried out on land, at sea, and in the air. For extensive areas, reconnaissance over both land and sea is conveniently done with an airborne magnetometer.

As in the case of gravity, the magnetic field anomaly is simply the observed minus the predicted value at the observation site. If $T_{obs}$ is the measured total field (corrected for temporal variation (diurnal correction)) and $T_R$ the reference field, given by the IGRF tables (International Geomagnetic Reference Field) at the site, the geomagnetic anomaly in the total field $\Delta T$, is given by $\Delta T = T_{obs} - T_R$. The advent of satellites dedicated to measuring the total field T or its vector components has remarkably augmented the global coverage and improved the data for analysis of the earth's field (the International Geomagnetic Reference Field is revised every five years). Observations of the $\Delta T$ anomaly field (or its vertical or horizontal component) over the area of the survey reflect subsurface variations in the magnetization of rock formations. Specific procedures such as derivatives and filtering procedures are useful in separating anomalies. Upward and downward continuation are also used for the determination of regional and residual. A special procedure is to reduce the field to the pole. It consists in the transformation of the anomaly observed at the survey latitude where the field is inclined in an anomaly that would be observed at the magnetic north.

For most applications of magnetic surveying, the magnetic effect of the sedimentary rocks may be considered as approximately the same as if the sediments were not present and the magnetic disturbances recorded have their origin at or below the base of the sediments. This is the basis for use of magnetic measurements to map the basement surface. The magnetic method is particularly suitable for mapping basement features such as lineament, faults, shear zones, lithologic contact, etc., which may be hidden from direct view because overlying sedimentary cover.

Figure 2.10b shows the magnetic anomaly after pole reduction (Girard, 2017) observed in Martique in the area investigated by a gravimetric survey (Figure 2.7). The volcanic material of various ages highlights generally various responses in link with the varying geomagnetic field.

For more information about the magnetic method, we recommend reading the book written by Fairhead (2015).

### 2.2.3 *Electrical and EM methods*

On the historical side, Electrical methods dedicated to Geosciences began with the Schlumberger Brothers in the late 20's. In a century, technology started from a simple DC resistivity method and went up to complex Electromagnetism methods implying natural or controlled sources, from 1D to 4D models, from acquisition in boreholes to land, air and sea. EM is now used in, tectonic studies,

Oil & Gas and Mining Industry, Geothermal and Near surface studies (civil engineering, groundwater monitoring and environmental purposes).

First known success occurred with mineral exploration on highly conductive sulfide metal ores bodies.

A behavior of an EM field is controlled by 3 main parameters:

- Electrical conductivity/resistivity
- Dielectric permittivity
- Magnetic susceptibility

The Electrical conductivity or resistivity is the most important for DC and low frequency methods (i.e. below 1 kHz for MT, AMT, mCSEM, AEM) whereas the Electric permittivity is the most important for high frequency methods (i.e. above 1 MHz for GPR).

The chart (Figure 2.11) shows that materials which are part of E&P investigations are distributed over a massive range of orders of magnitudes regarding electric resistivity. Resistivity variations in sediments are controlled by variations of porosity, permeability, pore connectivity geometry and the fluids contained by the pores.

As standard approximations, the industry often takes 0.3 Ω·m for seawater, 1.5 to 3 Ω·m for sediments saturated with brine and up to 100 Ω·m for hydrocarbon bearing reservoirs. Almost two orders of magnitude between sediments containing brine and those containing HC. On the other side, elastic waves could not even pretend to be 1 order of magnitude of difference.

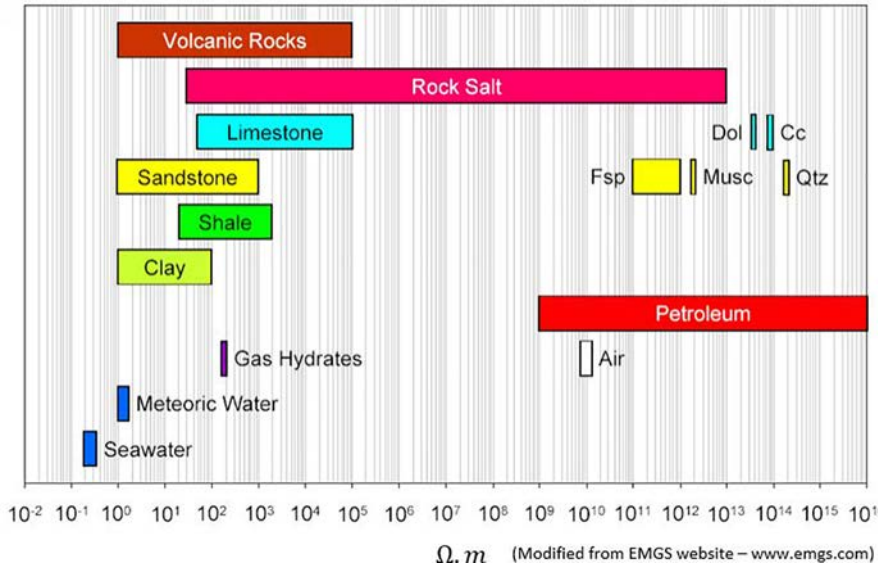


Figure 2.11 *Electric resistivity versus rock type.*

## Electrical methods

Electrical methods, in DC current, are based on the measurement from the surface of the apparent resistivities of the ground. Resistivity of geological formations can vary:

- from 1 to 10 ohm.m for clay and marl,
- from 10 to 100 ohm.m for sands and sandstone,
- from 100 to several thousands of ohm.m for limestone and the eruptive rocks,
- in practice DC currents are sent in formation using current electrodes A or B (Figure 2.12a).

The current sent by an electrode A(+) is collected by an electrode B(–), but according to the principle of superposition, the potential in a point M or N is the same one for a current I(+) independently sent by A or B. The measurement of the potential difference $\Delta V$ created by the passage of the current I between two electrodes M and N allows to estimate the resistivity $\rho$ of the formation (Figure 2.12b). If the formation is isotropic and homogeneous the measured resistivity is the true resistivity of the formation. If the ground is heterogeneous, the measured resistivity is an apparent resistivity, which is a function of the nature of the ground and the dimension of the array used. The array is conventionally a 4 electrodes array AMNB (Figures 2.12b and 2.12c), the depth of investigation of which being function of its characteristic length L (Figure 2.12c).

AMNB array, with constant distances between electrodes and a given characteristic length L, moved along profiles, is currently used to establish profiles or maps of resistivity, associated with a depth of about constant depth investigation. To investigate several depths, several profiles must be recorded with several characteristic lengths L (Figure 2.12d). Figure 2.12e shows an example of a resistivity map obtained with a characteristic length of 100 m.

A Schlumberger array with a constant distance between electrodes M and N and a variable increasing distance between electrodes A and B is used to obtain a distribution of resistivity versus depth. One of the limitations of the electrical soundings comes to the fact that they do not consider the horizontal variations of the resistivity of the ground.

Methods of electrical imagery 2D and 3D have been developed to obtain a model of the ground where the distribution of resistivities varies vertically and horizontally along the profile. 2D or 3D acquisitions generally use a great number of electrodes connected to multicore cables and placed along profiles. An acquisition device automatically selects the electrodes used for the injection of the current and for the measurement of the potential difference $\Delta V$. It also computes the distribution of apparent resistivities versus depth Z and distances X and Y, considering the different geometries of acquisition. In a next step, 2D or 3D iterative electrical tomographic inversion algorithms are used to obtain resistivity distribution in the 2D, or 3D space. The methodology, called electrical resistivity tomography ERT, requires an a priori distribution of resistivity used to initiate the inversion process. The process

works iteratively and stops when the updated distribution of resistivity allows to compute a set of apparent resistivities which fits, in a root mean square sense, the measured apparent resistivity distribution. Figure 2.13 shows an example of 2D electrical tomography, obtained on the rock glacier of Verbier in Switzerland. The example is a near surface example, with a depth investigation of 30 m.

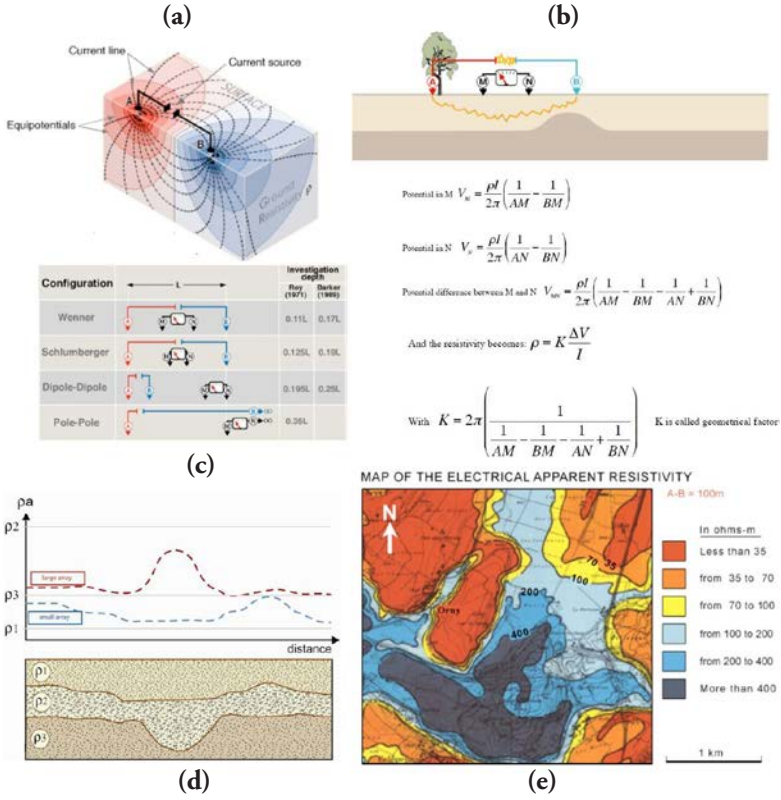


Figure 2.12 *Electrical method. After D. Chapellier (2001b). (a) Equipotential and current flow lines for two sources of current. (b) Measurement of apparent resistivity. (c) Depth investigation of the electrical method versus the spread configuration. (d) Resistivity profiles. (e) Electrical apparent resistivity map. Document IGL.*

For deep target, specific field apparatus has been developed (Carrier et al., 2019). It consists of a set of 2-channel independent receiving nodes called V-Fullwavers, one current measurement unit called I-Fullwaver, an induced polarization transmitter (VIP). Current is injected through the induced polarization transmitter. The transmitter enables to inject current up to 10 Amps, 5000 W and 3000 V, with a frequency of 0.5 Hz. The receiving nodes (V-Fullwavers) continuously record the electrical field and the injection electrodes can be moved inside and outside the receiving nodes with any type of electrode array configuration. For the field

example shown in Figure 2.14, the distance between 2 injection electrodes is 50 m, the distance between 2 receiving nodes is 100 m, the overall length of the profile is 4500 m. After electrical resistivity inversion, the resistivity section has a depth investigation of several hundred meters.

Electrical resistivity tomography (ERT) and Induced polarization (IP) surveys can provide resistivity, porosity, reaction temperature and cation exchange capacity (CEC) tomograms from surface measurements (Piolat et al., 2024). ERT/IP survey results for the Amashyuza geothermal prospect (Rwanda) are shown in Figure 2.15 (after Piolat et al., 2024). Electrical geophysical methods are of great value in this context, as they provide vital information on fluid flow networks, alteration intensity, hydrothermal temperatures, and geological identifications.

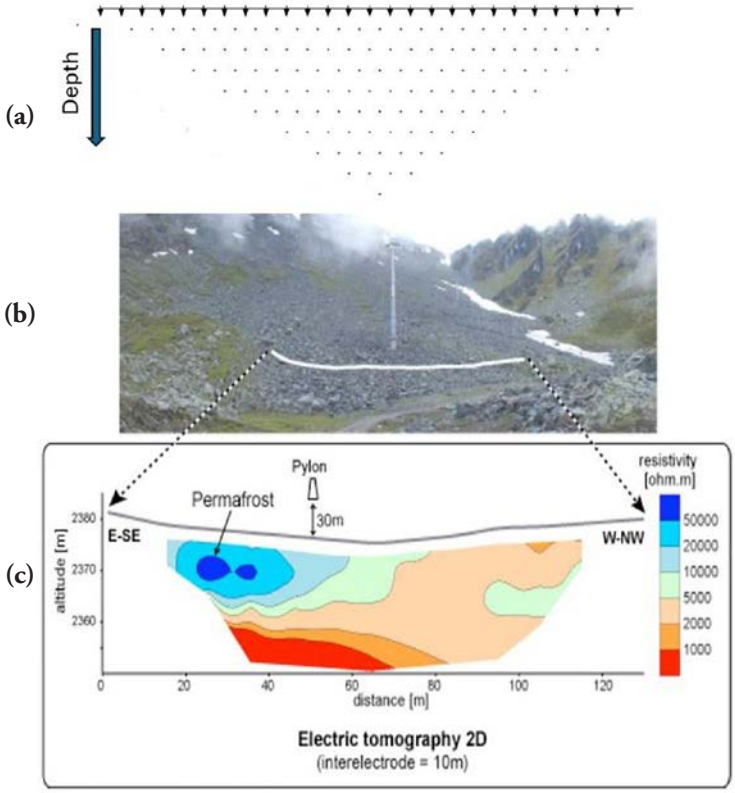


Figure 2.13 *Example of 2D electrical tomography, obtained on the rock glacier of Verbier in Switzerland. (a) line of electrodes (distance between two adjacent electrodes is 10 m) and theoretical location (indicated by dots) of apparent resistivity measurement depending on the array configuration, (b) view of the rock glacier of Verbier, c: resistivity section. After D. Chapellier (2001b, Document IGL).*

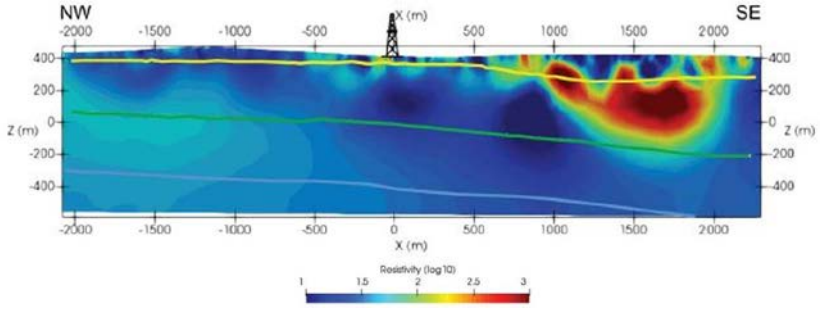


Figure 2.14 *Example of deep electrical resistivity tomography. After Carrier et al. (2019).*

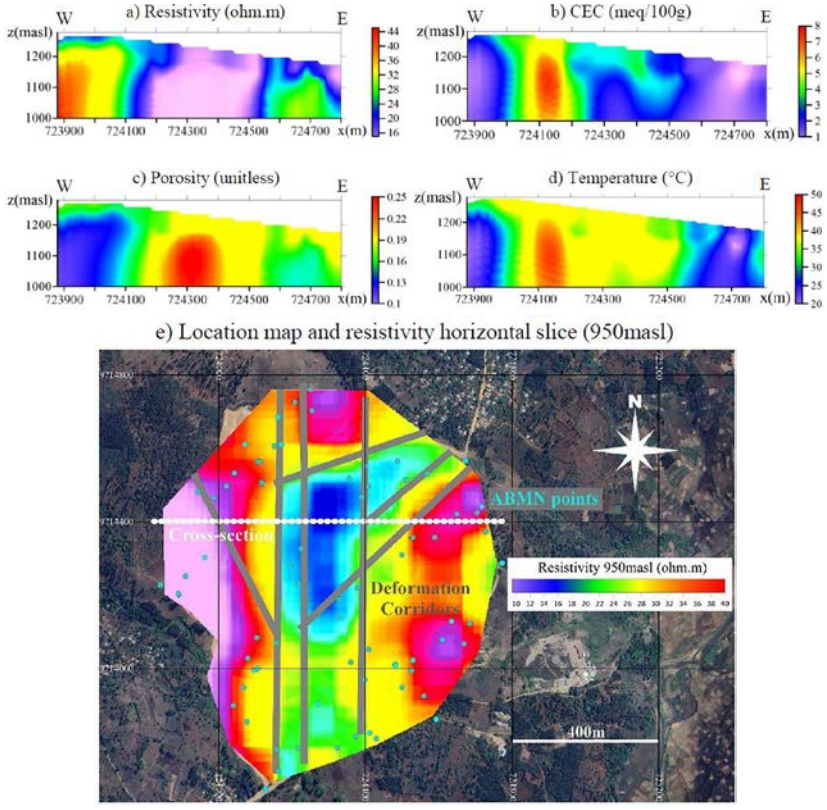


Figure 2.15 *DEEP-ERT cross-section results of resistivity (a), CEC (b), porosity (c), reaction temperature (d), and resistivity plan section (e) for the Amashyuza geothermal prospect in Rwanda (after Piolat et al., 2024).*

For more information, we recommend the reading of the part of the online course of geophysics (http://www-ig.unil.ch/), devoted to electrical methods.

## EM methods (AC)

Electromagnetism methods (EM) are based on the study of electromagnetic field generated either by natural or controlled sources.

With natural source (EM fields occurring naturally), the incident signal tends to behave like a plane wave at the air interface. The two components $E_x$ and $E_y$ of the electric field and the associated two components $H_x$, $H_y$ and potentially Hz components of the magnetic field are measured. The apparent resistivity already defined in the previous section (in ohm.m) of the subsurface structure is usually estimated:

$$\rho_{a,xy} = \frac{1}{2\pi f}\frac{|E_x|^2}{|H_y|^2} = \frac{1}{2\pi f}|Z|^2 \tag{2.10}$$

with Z, the impedance tensor, $E_x$ and $E_y$ the spectral horizontal components of the electric field expressed in V/m in the horizontal x and y directions, $H_x$ and $H_y$ the spectral horizontal components of the magnetic field expressed in A/m in the horizontal x and y directions, f the frequency in Hz. Inversion of apparent resistivity and phase of the impedance tensor, leads to earth resistivity model (2D and 3D).

With controlled sources, manmade electric dipoles, current loops, …, the two components $E_x$ and $E_y$ of the electric field and the associated two components $H_x$, $H_y$ of the magnetic field are measured. In some borehole applications, both vertical components: $E_z$ and $H_z$ can also be measured. The link between data and earth resistivity cannot be simplified anymore to the apparent resistivity concept, because the incident signal is not a plane wave anymore.

Natural or manmade sources, 2D and 3D interpretation of EM data requires the derivations of the Maxwell's equations (numerical modelling and inversion).

At those frequencies, the EM signal is strongly attenuated through a diffusion process. Such attenuation is controlled by the so-called skin depth:

$$\delta \approx 503\sqrt{\rho / f} \tag{2.11}$$

Skin depth is defined as the distance along which the electromagnetic field has reduced to $e^{-1}$ (or 37 percent) of its original amplitude value at the surface or source location. Signal penetration is therefore function of frequency and earth resistivity for natural source and also offset (distance in between source and receiver) for manmade source.

Active audiomagnetotellurics (AAMT), transient electro-magnetic (TEM), time domain electromagnetic method (TDEM), controlled source electromagnetics (CSEM) and controlled source audiomagnetotellurics (CSAMT) methods fall in the category of active EM methods.

Figure 2.16 is an example of receiver and dipole source for marine CSEM acquisition, the dipole source being towed behind the vessel and receivers dropped down on the sea floor.

Magneto-telluric (MT) and audio-magneto-telluric (AMT) methods fall in the category of passive EM methods with natural source. The origin of the variations of earth's magnetic fields, called magnetic micro-pulsation, is the ionospheric and

magnetospheric currents caused by plasma (solar winds) emitted from the sun and interfering with the earth's magnetic field. The micro pulsations induce eddy currents in the ground, called telluric currents, and their density and distribution depend on the local conductive structure of the ground. The natural EM-field has a very wide spectrum, low frequencies, from 0.0001 to 10 Hz are used in investigations for depths of several tens to hundreds of kilometers (actual MT method), while higher frequencies mostly due to lightning around the world, from 10 to 1000 Hz are used for shallower targets (audio-magneto-telluric method – AMT). MT, in association with gravimetric (Figure 2.7) and magnetic (Figure 2.10b) surveys, has been successfully used for geothermal exploration in Martinique (Girard, 2017).

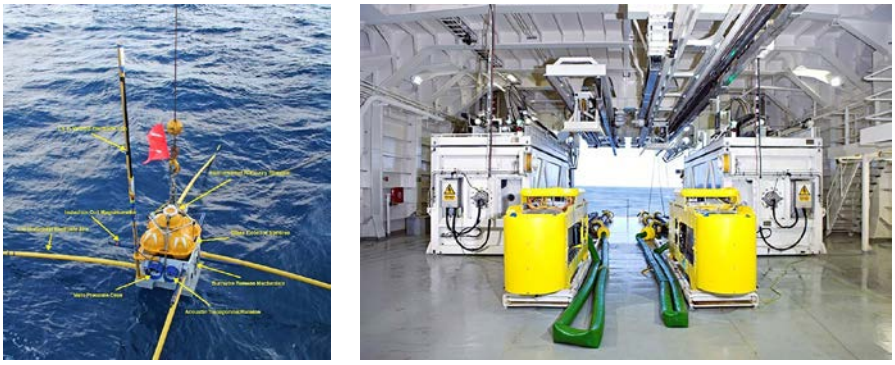

**(a)** **(b)**

Figure 2.16 *Receiver (a, courtesy of Cripps Institution of Oceanography) and dipole source (b, courtesy of EMGS) for marine CSEM acquisition.*

Figure 2.17 is an example of mCSEM (marine CSEM) from the Hoop area of the Barents Sea. The area in question covers a significant oil discovery in the Hoop Fault Complex on the Bjarmeland Platform in the Barents Sea, Norway (Alvarez et al., 2017). A densely sampled dataset consisting of six lines of 2D seismic and towed streamer CSEM data were acquired concurrently in 2015 by PGS. The survey area lies in water depths of approximately 400 m. Two public domain wells in the area provide calibration for the integrated analysis. Some mCSEM data acquired along line 5001, in the form of source gathers at 1 Hz are shown. A significant response to the accumulation encountered at Wisting Central can be clearly seen in the CSEM data, particularly in the phase response (Figure 2.17a, lower panel around 611 km Easting). This is observed across a wide band of frequencies.

The mCSEM data for six frequencies (0.2 Hz, 0.8 Hz, 1 Hz, 1.4 Hz, 2.2 Hz, 2.6 Hz) were inverted using an Occam approach (Constable et al., 1987; Key, 2016) to derive anisotropic resistivity models. The inversion was performed in stages. Firstly, an unconstrained inversion was run to examine the resistivity structure obtained in the absence of any a priori information. However unconstrained inversions in general have poor resolution. Resolution can be improved by including structural

information from the seismic data. This also ensures consistency between seismic and CSEM derived results, which is important for subsequent integrated interpretation. In this way, vertical (Figure 2.17b, upper panel) and horizontal (Figure 2.17b, lower panel) resistivity were recovered. Good RMS residual was achieved insuring that such recovered resistivity model honored the data.

Vertical resistivity for the unconstrained and constrained inversions run are shown in the interval of interest: the top one (Figure 2.17c, top) corresponding to the unconstrained

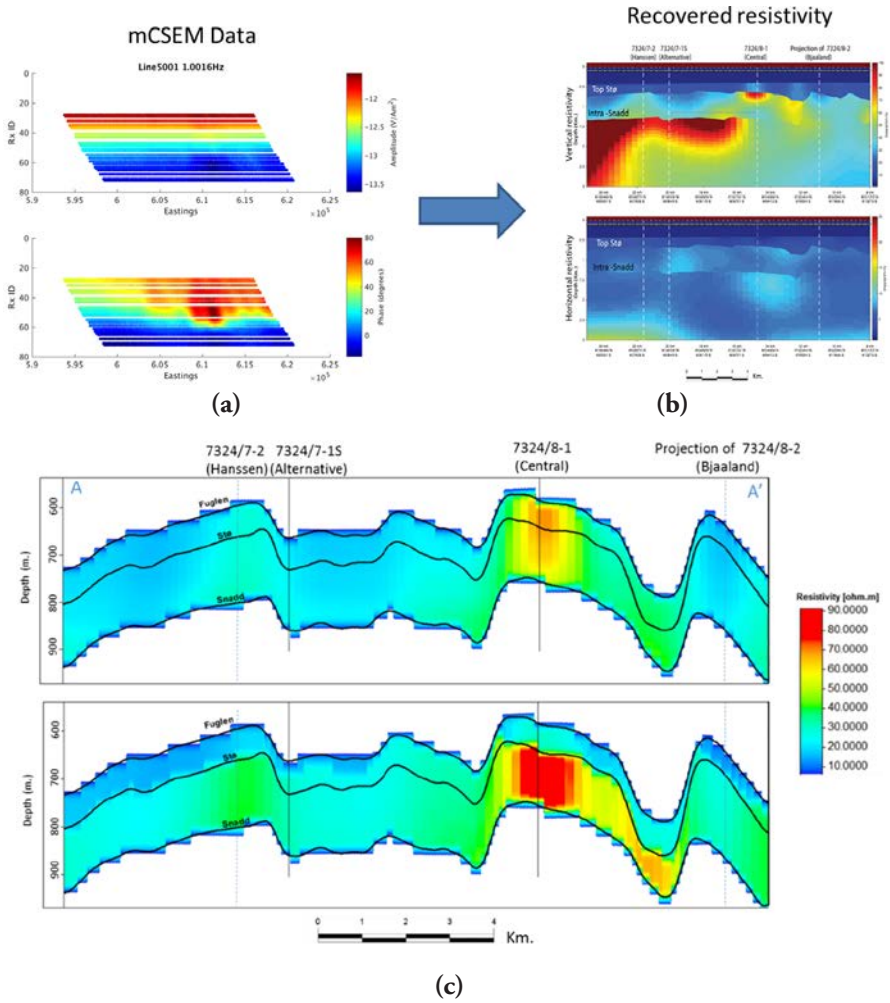


Figure 2.17 *mCSEM example from the Hoop area of the Barents Sea. After Alvarez et al. (2017). (a) mCSEM data in the frequency domain (amplitude (top) and phase (bottom)), (b) recovered resistivity results by seismically constrained inversion (vertical resistivity (top) and horizontal resistivity (bottom)), (c) vertical resistivity for the unconstrained (top) and seismically constrained (bottom) inversions run shown in the interval of interest.*

inversion, and the bottom image (Figure 2.17c, top) shows the results of the constrained inversion previously shown. Both models are equivalent mCSEM wise (same mCSEM data fit) as they have the same transverse resistance (integration of the resistivity with respect to depth). The constrained results are preferred given the a priori information available. A qualitative interpretation of the CSEM inversion results supports the outcome of the Alternative, Central and Bjaaland wells. A prominent resistivity anomaly is recovered at Central, in which there was a significant oil discovery, which agrees with the high resistivity values measured at the reservoir location. On the other hand, the Realgrunnen structures penetrated at Alternative and Bjaaland, two dry wells, are related to low resistivity values that support the petrophysical outcome. Such analysis of the CSEM data in isolation does not allow to go beyond the previous qualitative conclusion. Only a quantitative approach that integrates the resistivity measurements with the seismic analysis can lead to reservoir properties

Figure 2.18 is an MT example (Avram, 2017). Uzbekistan, along with Russia and other FSU countries have long histories deploying MT measurements on their oil and gas fields especially for those one that are poorly covered by seismic. In the example, Uzbekgeofizyka partnered with Phoenix Geophysics deployed a very large, dense MT survey over East Buzakhur. The results shown here concern the East Buzakhur – Karabay contact (Figure 2.18a).

MT was tasked with the following:

1. bring additional information regarding the extent of the hydrocarbon system West of the main fault,
2. confirm and map the faults that control the East extent of the hydrocarbon system,
3. bring additional information that better characterize the source of these systems, their origin, and their relations from one basin to the next one, if any.

After data analysis and preprocessing, the MT resistivity pseudo sections are converted in resistivity by inversion (Figure 2.18b). The data analysis has put into evidence the following: MT responses have different behavior whether they are collected over the known deposit or away from it. The main structural N-S fault is visible and seems to control the Eastern trap of the reservoir.

mCSEM is best suited for deep waters acquisition layout. Shallow waters could lead to absence of sensitivity to resistive targets. Resolution of mCSEM is lower than for reflected amplitude seismic methods, but better than for potential fields methods. Transmitter frequencies must be chosen regarding target depth and host rock resistivity, keeping in mind skin depth concept. MT data could help to invert mCSEM data to image subsurface resistivities distribution. Combination of MT and gravity methods can be used in a Multiphysics approach to reduce the uncertainties and enhance resolution (Ceci et al., 2024a,b).

For more information, we recommend the reading of the e-book devoted to electromagnetic methods in geophysics (http://books.ifpenergiesnouvelles.fr/ebooks/ifpen-electro/).

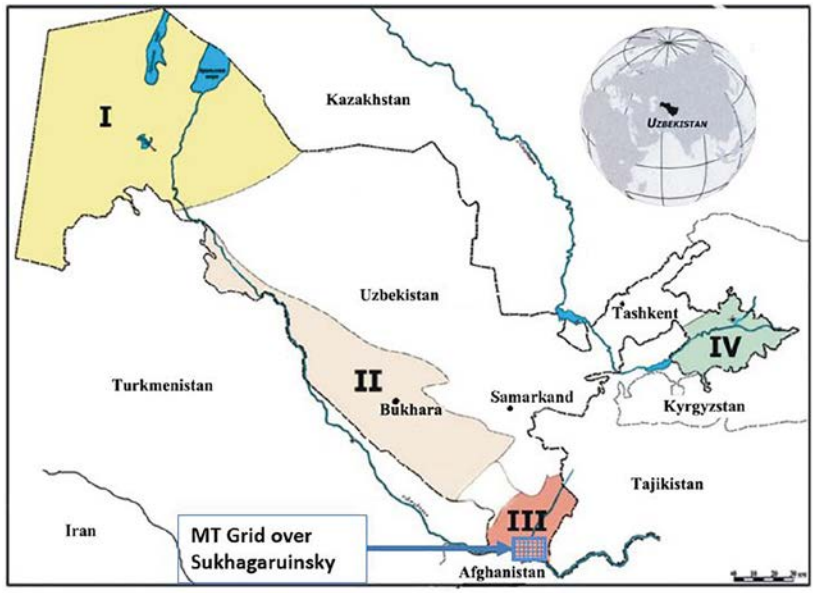


**(a)**

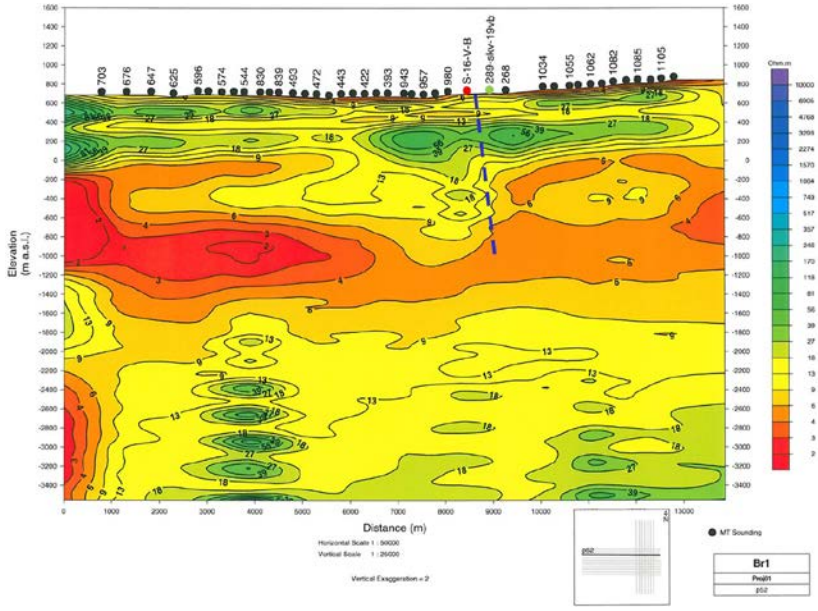


**(b)**

Figure 2.18 *MT example in Uzbekistan. After Avram (2017), courtesy of Phoenix Geophysics. (a) Major Mesozoic hydrocarbon bearing basins in Uzbekistan and location map of the MT survey, (b) MT resistivity pseudo sections converted in resistivity by inversion.*

### 2.2.4 *Seismic methods*

Seismic prospecting consists of generating very low-amplitude artificial earthquakes at predetermined times and positions. The seismic disturbances generated by a seismic source are recorded by a seismic receiver spread. The acquisition geometry is defined by the distribution of the source spread and the receiver spread.

The following elements are needed to observe the propagation of seismic, acoustic, or elastic waves:

1. A source spread. The source is a device capable of producing a deformation in a medium. In land acquisition, it can be an explosive charge (dynamite), a weight dropper or a vibrator. In marine acquisition, it can be an air gun, a sparker, or a vibrator. Seismic energy radiated by the source is split between body waves (compressional P and shear S waves) and surface waves.

   A P-wave has a particle motion parallel to the direction of propagation. A S-wave has a particle motion perpendicular to the direction of propagation. P and S waves propagate at $V_P$ and $V_S$ velocities respectively. When a P- or S- wave strikes an interface at some angle of incidence not equal to zero, four waves are generated: two transmitted (one P- and one S-wave) and two reflected (again one P- and one S-wave).The angular relationships between the propagation directions of each of these waves are given by Snell's law (Figure 2.19a). When P- or S-waves strike the interface at the critical angle $i_c$, head waves or refracted waves are generated. This only occurs when a wave perturbation passes from a medium with velocity $V_i$ to another with velocity $V_{i+1}$ which is greater than $V_i$ and at the critical angle given by $\sin(i_c) = V_i/V_{i+1}$.

   The critical angle $i_c$ is the criterion for differentiating the various seismic methods associated to body wave propagation (Figure 2.19b):

   - $i < i_c$: the method is seismic reflection,
   - $i = i_c$: the method is seismic refraction,
   - $i > i_c$: the method is wide angle reflection. In wide angle reflection there is no transmitted energy, only reflected.

2. A physical medium defined by its geometric and mechanical characteristics. Here we consider the geological formations defined by the following mechanical properties:

   - propagation velocity of the compressional P-waves in the rock: $V_P$ (expressed in m/s),
   - propagation velocity of the shear S-waves in the rock: $V_S$ (expressed in m/s),
   - density $\rho$ (expressed in $g/cm^3$ or $kg/m^3$),
   - quality factor Q which characterizes the ability of the rock to absorb seismic energy: a higher value indicates lower absorption of seismic energy. Sedimentary rocks have Q ranging from about 10 to several hundred.

3. An elastic deformation of the medium after the initial shaking caused by the source. A deformation is considered elastic when the medium returns to its

original state after the causes of deformation have disappeared, i.e. when the medium has not been damaged by the wave passing through it.

4. A receiver spread. It is capable to record the deformations generated by the source after propagation in the geological medium:
   - either by variations in the displacement, velocity, or acceleration of particles (geophones, accelerometers),
   - or by pressure variations (hydrophones).

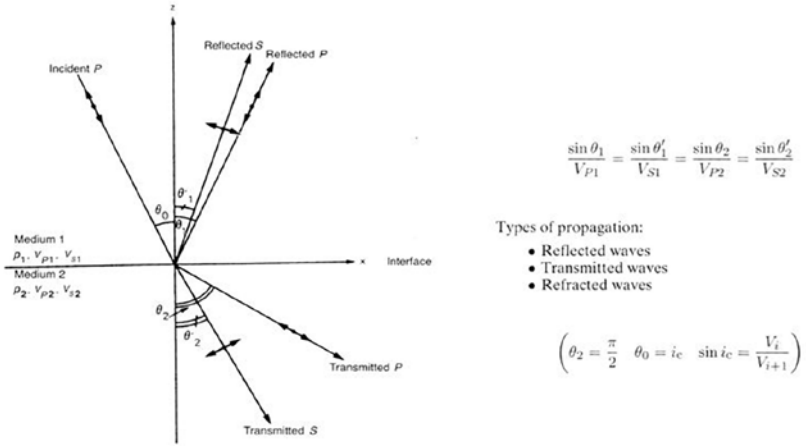


$$\frac{\sin\theta_1}{V_{P1}} = \frac{\sin\theta'_1}{V_{S1}} = \frac{\sin\theta_2}{V_{P2}} = \frac{\sin\theta'_2}{V_{S2}}$$

$$\left(\theta_2 = \frac{\pi}{2} \quad \theta_0 = i_c \quad \sin i_c = \frac{V_i}{V_{i+1}}\right)$$

**(a)**

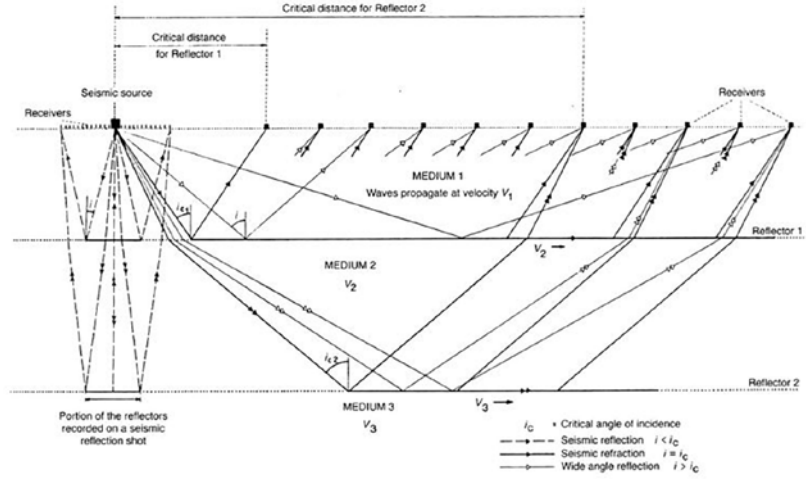


**(b)**

Figure 2.19 *Seismic wave propagation. (a) Snell's law, after Lavergne (1986), (b) the various types of seismic surveying versus critical angle.*

Figure 2.20 gives the range of values of propagation velocities, $V_P$ and $V_S$, and densities of the principal rock types. It also gives the expressions of the main mechanical modules (Poisson's coefficient, Young's modulus).

| **Type of rock or medium** | ***P*-velocity** $V_P$ (m/s) | ***S*-velocity** $V_S$ (m/s) | **Density** $\rho$ (g/cm$^3$) |
|---|---|---|---|
| Weathered rocks | 300 – 700 | 100 – 300 | 1.7 – 2.4 |
| Dry sands | 400 – 1200 | 100 – 500 | 1.5 – 1.7 |
| Wet sands | 1500 – 4000 | 400 – 1200 | 1.9 – 2.1 |
| Clay | 1100 – 2500 | 200 – 800 | 2.0 – 2.4 |
| Marl/shale | 2000 – 3000 | 750 – 1500 | 2.1 – 2.6 |
| Sandstone | 3000 – 4500 | 1200 – 2800 | 2.1 – 2.4 |
| Limestone | 3500 – 6000 | 2000 – 3300 | 2.4 – 2.7 |
| Chalk | 2300 – 2600 | 1100 – 1300 | 1.8 – 2.3 |
| Salt | 4500 – 5500 | 2500 – 3100 | 2.1 – 2.3 |
| Anhydrite | 4000 – 5500 | 2200 – 3100 | 2.9 – 3.0 |
| Dolomite | 3500 – 6500 | 1900 – 3600 | 2.5 – 2.9 |
| Granite | 4500 – 6000 | 2500 – 3300 | 2.5 – 2.7 |
| Basalt | 5000 – 6000 | 2800 – 3400 | 2.7 – 3.1 |
| Coal | 2200 – 2700 | 1000 – 1400 | 1.3 – 1.8 |
| Water | 1450 – 1500 | – | 1 |
| Ice | 3400 – 3800 | 1700 – 1900 | 0.9 |
| Oil | 1200 – 1250 | – | 0.6 – 0.9 |

First Lamé parameter $\lambda = \rho\left(V_P^2 - 2V_S^2\right)$

Shear modulus (or second Lamé parameter) $\mu = \rho\, V_S^2$

Poisson's coefficient $\sigma = \dfrac{\gamma^2 - 2}{2\,(\gamma^2 - 1)}$ where $\gamma = \dfrac{V_P}{V_S}$

Young's modulus $E = \rho V_P^2 \dfrac{(1 - 2\sigma)(1 + \sigma)}{1 - \sigma}$

Bulk modulus $K = \rho\left(V_P^2 - \dfrac{4}{3}V_S^2\right)$

Figure 2.20 *Seismic velocities and densities, mechanical modules. After Lavergne (1986).*

A seismic spread is composed of a source spread and a receiver spread. In 2D seismic survey, the sources and the receivers are located on the same line which defines a 2D seismic profile. In 3D seismic survey, the sources and the receivers are usually located on 2 orthogonal lines: a line of sources and the line of receivers. A seismic record is a set of seismic traces recorded at different receiver positions. The seismic trace represents the vibrations of the ground due to wave propagation generated by a seismic source. On a field record, the geophysicist can identify the different seismic waves (Figure 2.21). Figure 2.21 shows examples of 2D and 3D records.

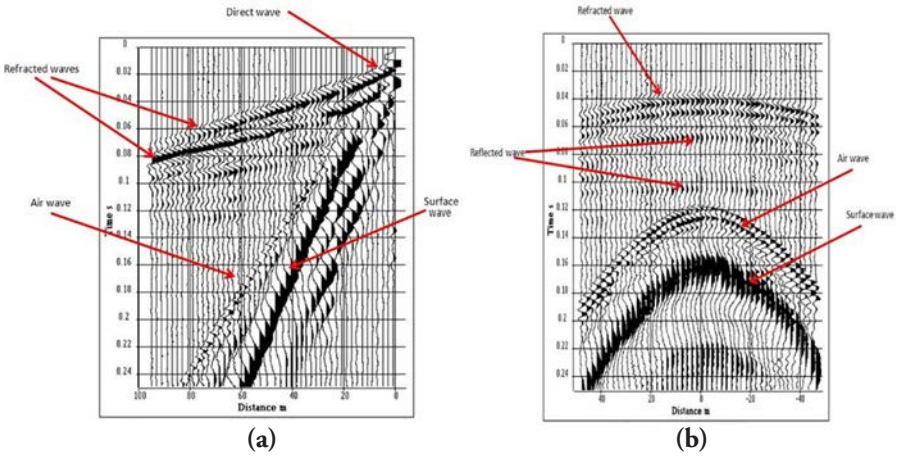


Figure 2.21 *Examples of 2D (a) and 3D (b) seismic records. After Mari and Mendes (2019).*

In addition to body waves (P- and S-waves) which propagate within the subsurface, a surface seismic source generates surface waves (Love and Rayleigh waves). These waves are used in civil engineering to determine the mechanical parameters (shear velocity and shear modulus) of the first tens of meter below the ground surface. The seismic method based on the analysis of surface waves is called MASW (Multiple Analysis of Surface Waves).

For more complete information on wave propagation, the reader is invited to consult other works such as Achenbach (1973), Lavergne (1986), Dobrin and Savit (1988), Quiblier (1997), Mari and Mendes (2019).

Today, seismic acquisitions are done with recording systems which can simultaneously record seismic vibrations on several hundreds of sensors. The distance between two adjacent sensors must be chosen small enough to have correctly sampled data and avoid any phenomenon of spatial aliasing. Consequently, the different types of waves are correctly recorded, and the same seismic record can be used whatever the seismic method.

## Refraction seismic method

Today, the refraction method is a quick reconnaissance-mapping tool for delineating near-surface velocity structures. It requires only the measurement of arrival times of first arrival waves (direct and refracted waves) to provide a geologic model while the reflection methods require a complete processing of the recorded wavefield. Picking of first arrivals is much easier than identifying and picking of other events.

Seismic refraction is currently used in civil engineering and hydrogeology for objective depths less than 300 m (Mari et al., 1997). The method is particularly suited for the following studies:

In civil engineering for:

- preliminary studies for construction sites,
- determination of the near surface structures,
- rock mechanics (rippability, Poisson ratio),
- search for cavities.

In hydrogeology for:

- highlighting channels carved in the bed rock,
- highlighting fractured areas in the bed rock,
- measurement of the water table depth.

Refraction-based velocity estimation of the subsurface can be conventionally done by using well-known methods, such as the Hagedoorn's Plus-Minus method (1959) or the generalized reciprocal method (GRM) proposed by Palmer (1986), which gives simple models of the subsurface defined by refractors with simple geometry and mainly constant velocity distribution. The GRM method, widely used in refraction prospecting requires direct and reverse shots. It assumes that first-arrivals are only originated by critical refraction and lateral continuous refractors with relatively simple velocity distributions. It assumes small lateral variation and it is used to define refractors with simple geometry and mainly constant velocity distribution.

Picked times of direct and reverse shot points (Figures 2.22a and 2.22b) give access to the t plus ($t^+$) and t minus ($t^-$) curves which allow the computation of the refractor velocity analysis function, and the generalized time-depth or delay time, respectively.

The refractor velocity analysis function $t_{V,}$ at position G (Figure 2.22c), is defined by the equation:

$$t_V = \frac{1}{2} t_G^- = \frac{1}{2}(t_{AY} - t_{BX} + t_{AB}) \tag{2.12}$$

This function is computed for each pair of forward and reverse arrival times, $t_{AY}$ and $t_{BX,}$ and the reciprocal time, $t_{AB}$. The value of the function $t_V$ is referenced to G which is midway between X and Y, and it is plotted as a function of the distance AG. Considering a multi-layer model, the $t_V$ curve is approximately a linear function (Figure 2.22d), the slope $1/V'_n$ of which gives an apparent velocity $V'_n$ which approximates the velocity $V_n$ of the refractor.

The generalized time-depth or Delay, at position G (Figure 2.22c), is defined by:

$$t_G = \frac{1}{2} t_G^{+} = \frac{1}{2}\left(t_{AY} + t_{BX} - \left(t_{AB} + XY/V_n^{'}\right)\right) \quad (2.13)$$

The Plus-Minus method (a simplified version of the GRM method with XY = 0) assumes that first-arrivals are only originated by critical refraction and laterally continuous refractors with relatively simple velocity distributions.

Figure 2.22 is an example of a refraction survey. The refraction line is rectilinear. In the acquisition of data, a 48-channel recorder was used. An explosive source (25 g) was detonated and a single geophone (10 Hz) per trace was deployed. Such a source makes it easy to identify and pick first arrivals. The distance between two adjacent geophones was 5 m. A direct shot and a reverse shot were recorded (Figures 2.22a and 2.22b). To obtain the velocity of the refractor (top of the reservoir) and its depth, the Plus– Minus method has been used. It requires recordings where geophones are aligned with shot points. The arrival times of the direct and refracted waves have been picked on the two in line shots. The picked times from the in-line shots (direct and reverse) have been used to compute the t plus and minus curves to obtain the velocity V2 of the refractor and the generalized time-depth curve. The t minus curve (Figure 2.22d) can be approximated by a straight line, the slope of which gives the velocity of the refractor which was found to be 3350 m/s. The slope of the direct wave gives the velocity V1 of the medium situated above the refractor. The medium situated above the refractor is defined as the weathering zone (Wz). Its velocity was found to be 850 m/s. The generalized time-depth, also called Delay time, shows the shape in time of the refractor (Figure 2.22d).

The University of Poitiers (France) has developed a Hydrogeological Experimental Site (HES, Figure 2.23a) for the sole purpose of providing facilities to perform long-term monitoring and experiments for a better understanding of fluid flow and transfers in fractured rocks (Bourbiaux et al., 2007).

Due to the limitations of the area, the length of the seismic line could not exceed 250 m in the in-line direction. In the crossline direction, the extension of the area does not exceed 300 m. As a result, 20 receiver lines have been implemented, with a 15 m distance between adjacent lines. Figure 2.23b shows the map locating the seismic lines. In the acquisition of data, a 48-channel recorder was used. An explosive source (25 g) was detonated and a single geophone (10 Hz) per trace was deployed. Such a source makes it easy to identify and pick first arrivals. A 5 m distance between two adjacent geophones was selected to avoid any spatial aliasing.

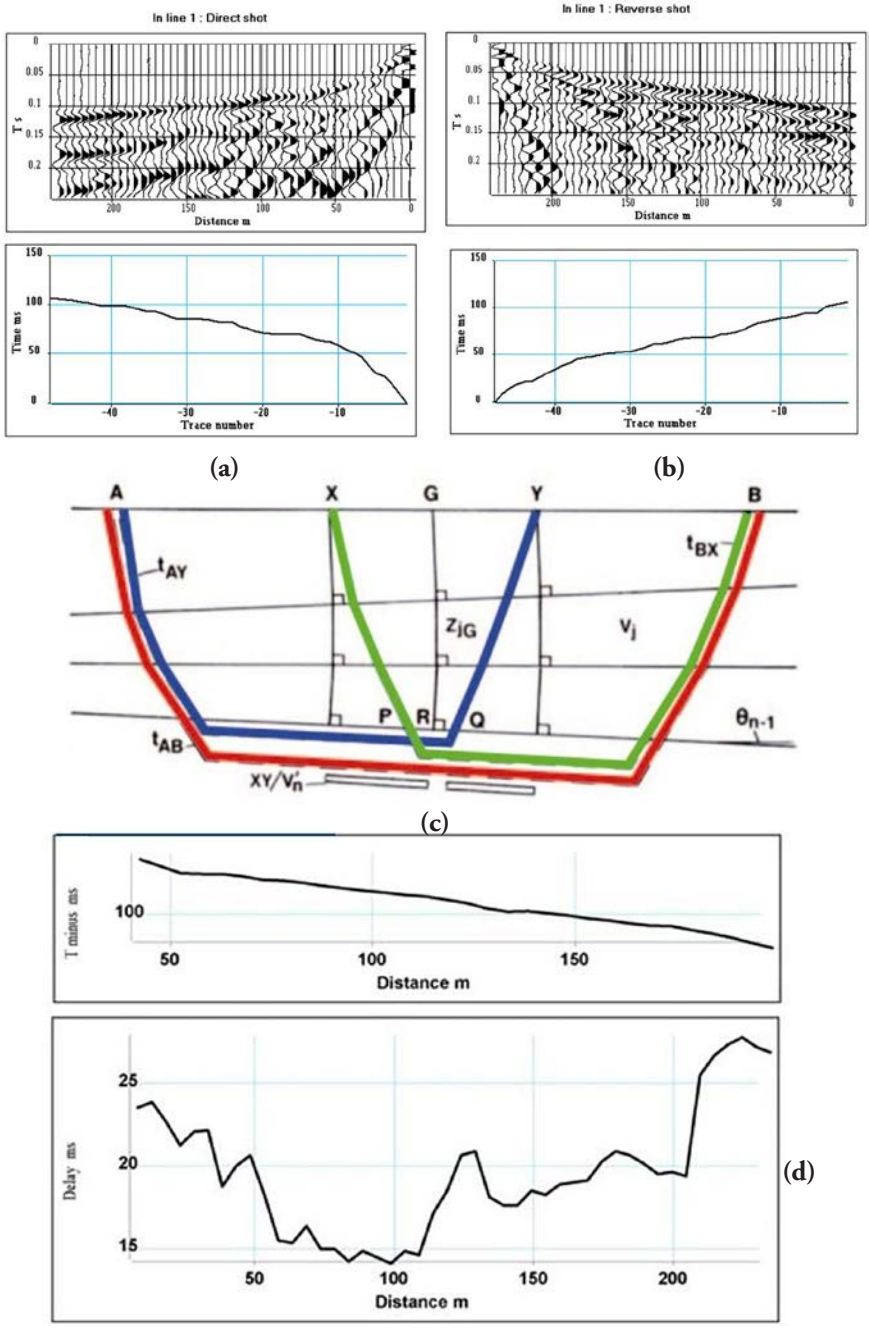


Figure 2.22 *GRM method. (a) and (b) Direct and reverse shots with first arrival picked times, (c) refracted wave raypaths, (d) T minus and delay curves. After Mari and Mendes (2019).*

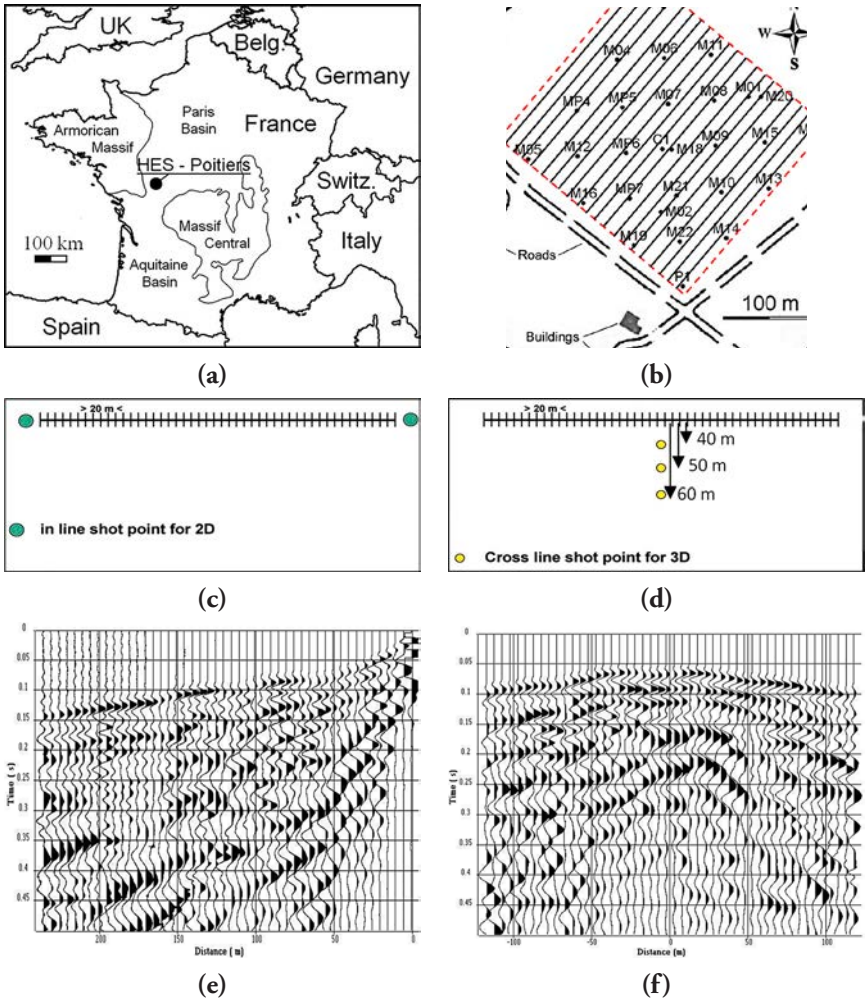


Figure 2.23 *Hydro-geological experimental site in Poitiers; (a) location map, (b) seismic line implementation. Seismic acquisition: (c) 2D in line acquisition geometry, (d) 3D cross line acquisition geometry, (e) example of in line shot gather, (f) example of cross line shot gather with 60 m of lateral offset. After Mari and Mendes (2019).*

A direct shot and a reverse shot were recorded per receiver line (Figure 2.23c). Three shot points in the crossline direction were fired at distances of 40, 50 and 60 m from the receiver line under consideration (Figure 2.23d). Figure 2.23e shows an example of an in line shot gather and Figure 2.23f a cross line shot gather with a lateral offset of 60 m. The picked times of the first seismic arrivals on all the shots (in line and cross lines shots), the Wz depth map and the velocity model obtained by the Plus–Minus method are input data for the inversion procedure, called tomography which is appropriate to obtain the velocity distribution in depth (Mendes, 2009; Mari and Mendes, 2012).

Figure 2.24 shows the velocity distribution at different depths (15 and 20 m), the 2500 m/s iso-velocity depth map, and a 3D block with vertical velocity sections located at a 0 m, 60 m, and 180 m distance in the crossline direction and velocity map located at 20 m in depth.

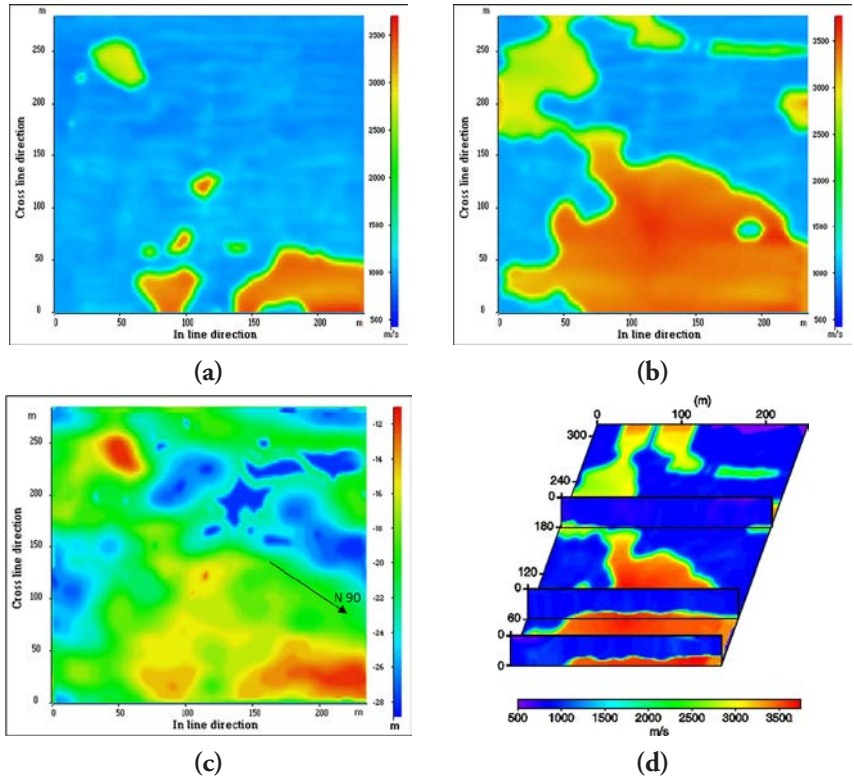


Figure 2.24 *Results of 3D tomography. (a) Velocity distribution at 15 m in depth, (b) velocity distribution at 20 m in depth, (c) 2500 m/s iso velocity depth map, (d) 3D block with vertical velocity sections located at a 0 m, 60 m, and 180 m distance in the crossline direction and velocity map located at 20 m in depth. After Mari and Mendes (2019).*

## Reflection seismic method

Seismic reflection is the most widely used seismic technique which has the advantage of providing a picture of the subsurface in two or three dimensions (2D or 3D) in a regular grid (Figure 2.25).

3D data are now increasingly used for field development and production and not only as an exploration tool. Pre-planning of the 3D surveys became then

a fundamental step to ensure the 3D data quality will meet structural, stratigraphy and lithology requirements. Pre-planning includes the evaluation of both geophysical and non-geophysical parameters such as environment considerations, health and safety requirements, etc. Specific pre-planning tools (Cordsen et al., 2000) were developed to estimate all characteristics of the future acquisition such as offset, fold and azimuth distributions, effects of surface obstacles, make up shots, etc. The pre-planning aims at defining the geological targets of the 3D with the associated geophysical parameters, design and costs.

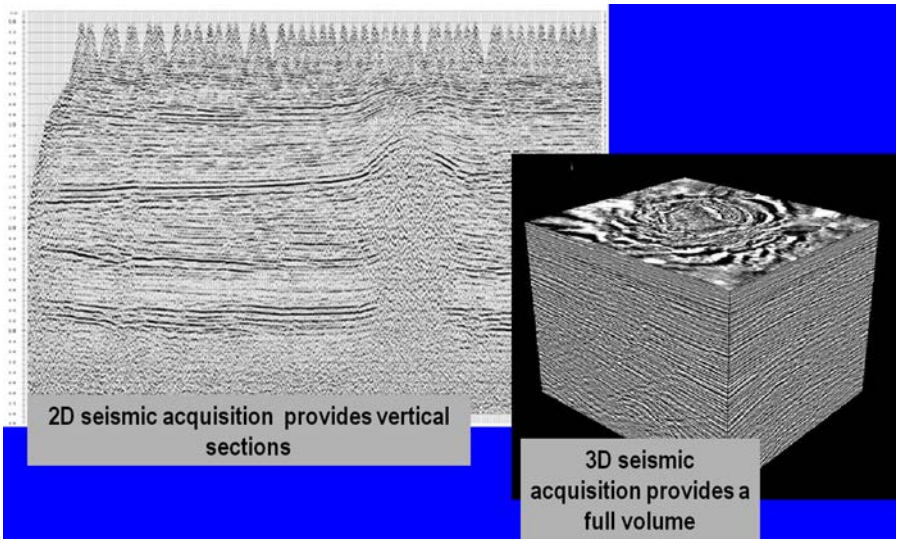


Figure 2.25 *2D and 3D seismic imaging (after J. Meunier, 1998, 1999, IFP School course).*

In 2D the image obtained after processing is a vertical seismic section. The horizontal axis of the section represents the geographical abscissas of subsurface points along the acquisition profile and the vertical axis represents the record time. The seismic events that appear on the records correspond to the arrivals of waves reflected at normal incidence on the seismic horizons. The seismic horizons correspond to discontinuities of acoustic impedance; their picks provide a structural image of the subsurface.

3D seismic acquisition provides a full volume consisting of a collection of sections parallel to each other. Surface seismic has vertical and horizontal resolutions measured in tens of meters with lateral investigation distances only limited by the size of the area investigated by the seismic surveys.

2D seismic acquisition is achieved with spreads which are either end-on also called off-end or split dip spread (Figure 2.26a). The individual shot element is defined by the source to the first receiver distance, the number of receivers and the distance between two adjacent receivers. A receiver can be a single sensor (geophone for

land acquisition) or an array of sensors. If the receiver is a single sensor, the interval between 2 receivers is of several meters, if it is an array, the interval is of several tens of meters. The maximum source-receiver offset to the far receiver is about the same as the maximum depth of the geological objective. The offset of the near receiver is chosen to minimize interference between ground roll (surface waves) and the reflection arrivals.

Acquisition is more complex for land 3D. Source and receiver lines are laid out to provide the most homogeneous coverage. The more conventional implementation is the cross-spread design with lines of sources perpendicular to lines of receivers (Figure 2.26b).

In 2D or 3D, the number of times a reflecting point in the sub surface is reached by different raypaths associated with different source-receiver pairs provide the fold of seismic coverage. Such a gathering, called Common Midpoint point (CMP), is theoretically valid for flat and horizontal geological models. In 2D, the distance between two CMP is equal to half the receiver interval. In 3D, the CMP is replaced by a cell or bin, the size of it being the product of half the source interval by half the receiver interval (Figure 2.26b). Traces contributing to the same CMP bin have irregularly distributed azimuths and offsets. Implementation is optimized to ensure the most regular azimuth and offset distribution possible. In the case of complex geological structures, the CMP is replaced by a common image gather.

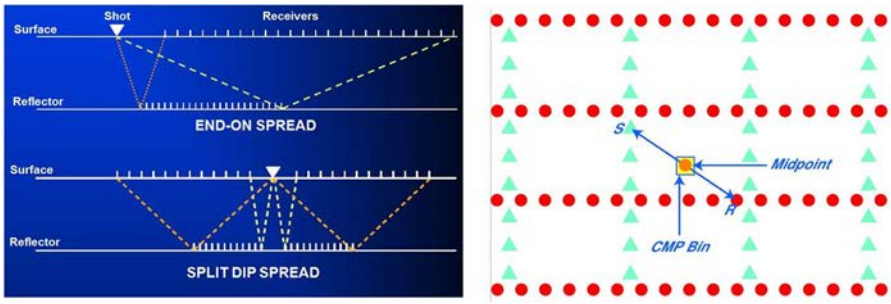


Figure 2.26 *Seismic spread; (a) in 2D, (b) 3D (lines of sources are indicated by green triangle, lines of receivers are indicated by red points). After Mari and Mendes (2019).*

The reader will find more information about acquisition and survey design in Galbraith (2000), Lansley (2000), Mayne (1962), Meunier and Gillot (2000), Meunier (2011), Monk and Yates (2000), Musser (2000), Vermeer and Hornman (2000), Chaouch and Mari (2006), about signal processing in Mari (2011), and about seismic processing in Yilmaz (1987), Robein (2003).

The classical approach to seismic processing can be summarized in two main steps.

The first step includes pre-processing of the data and the application of static corrections. The purpose of pre-processing is to extract reflected waves from individual shots, by filtering out the waves which are not reflected waves: direct and refracted arrivals, surface waves, converted waves, and noise. The conventional wave separation methods are the F-K method and the SVD method (Singular Value Decomposition). Pre-processing is intended to compensate for amplitude losses related to propagation. Deconvolution operators are applied to improve resolution (as example spiking deconvolution), harmonize records by considering source efficiency variations and eventual disparities between receivers, and attenuate multiples (predictive deconvolution). Any deconvolution is sensitive to noise. Some specific processes, such as SVD decomposition, are used to enhance signal to noise ratio, by splitting the data in a noise space and a signal space. Static corrections, that are specific to land seismic, are intended to compensate for the effects of the weathered zone and topography. Records are then sorted in common mid-point gathers or common offset gathers.

The second processing step is the conversion of common mid-point gathers or common offset gathers into time or depth migrated seismic sections. This second step includes the determination of the velocity model, with the use of stacking velocity analyses, or tomography methods. The role of migration is to place events in their proper location and increase lateral resolution, by collapsing diffraction hyperbolas at their apex. Proper migration requires the definition of a coherent velocity field, which must be a field of actual geologic velocities in migrated positions. Determination of the velocity field is the most critical aspect of migration. The migration process can be done post or pre stack in time or depth. After migration, vertical and horizontal resolutions can be estimated by a quarter of the dominant wavelength of the seismic signal. An inversion process can be applied to post stack migrated sections to recover acoustic impedance distribution Ip ($Ip = \rho V_P$, with $\rho$ density and $V_P$ P-wave velocity of the formation). An inversion process, which considers the amplitude variations versus offset of the reflected signal, can be applied to pre stack migrated sections to recover elastic impedance distributions Ip and Is ($Ip = \rho V_P$, $Is = \rho V_s$ with $\rho$ density, $V_P$ and $V_S$ respectively P-wave and S-wave velocities of the formation).

Figure 2.27 is an example of 3D seismic spread for near surface imaging.

The seismic spread is composed of a receiver spread and a source spread (Figure 2.27a). The receiver spread, displayed in green, is composed of 2 receiver lines. Receiver line direction is called the in-line direction. Distance between receiver lines is 4 m. There are 24 geophones per line. Distance between geophones is 2 m. The source spread, displayed in yellow, is composed of 11 source lines oriented perpendicularly to the receiver lines. 11 shots are fired per line. Distance between shots is 2 m. Distance between source lines is 4 m. The source lines and the receiver lines are oriented perpendicularly. The distance between receiver spread and source spread is 4 m. There is no overlap between the source and the receiver spread. Due to the geometry of acquisition, the geometry fold is symmetric. Figure 2.27b shows the fold variation. It varies from 0 to 22.

The processing has been done with the SPW software developed by Parallel Geoscience. The listening time is limited to 250 ms, the sampling time interval is 0.5 ms. Figure 2.28 is an example of shot point.

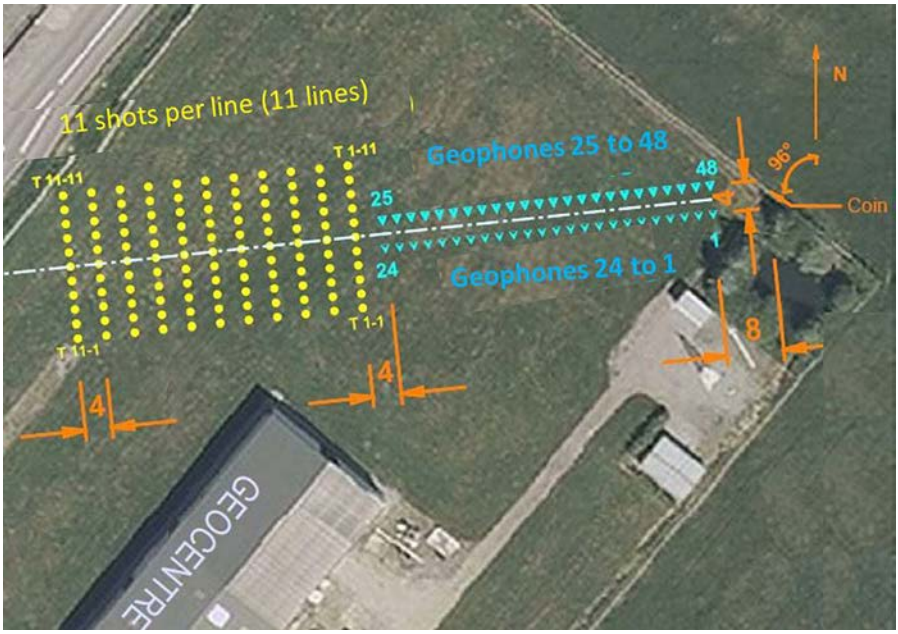


**(a)**

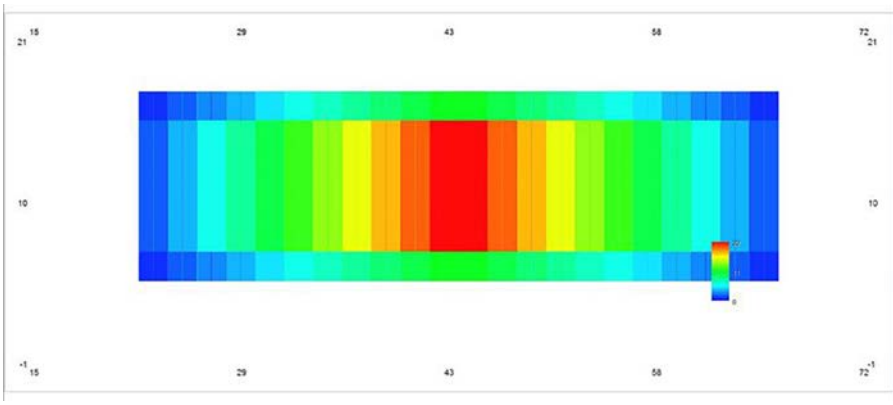

**(b)**

Figure 2.27 *Near surface imaging. (a) 3D seismic spread, (b) fold variation. It varies from 0 to 22. In the display, the horizontal axis is the in-line direction. The vertical axis is the crossline direction. After Mari and Mendes (2019).*

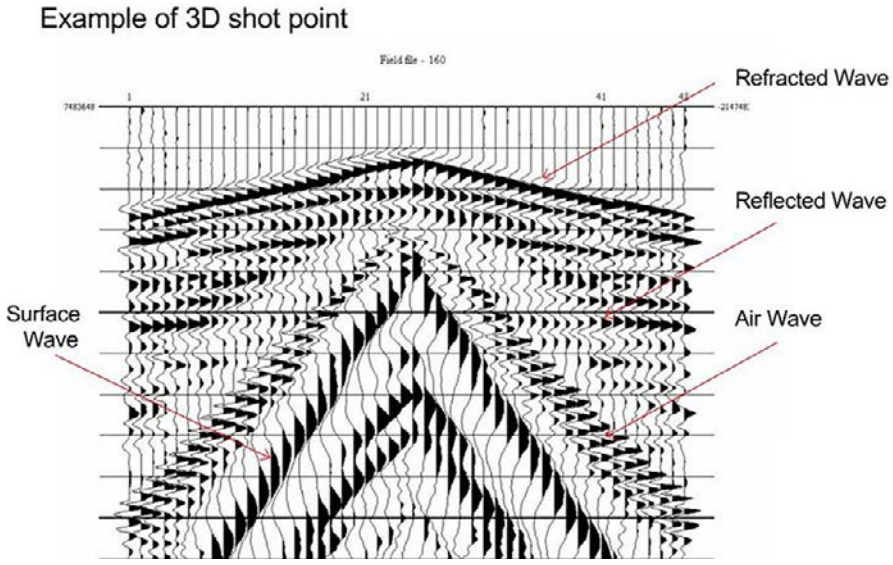


Figure 2.28 *Example of a 3D shot point. You can see the refracted wave, the reflected wave, the air wave, and the surface wave. The air wave is aliased. After Mari and Mendes (2019).*

The processing sequence of each shot includes amplitude recovery, deconvolution in the 15–150 Hz frequency bandwidth, tail mute, static corrections computed with the GRM method. The deconvolution is done to increase the resolution and attenuate the surface waves. A tail mute is used to kill the air waves and the surface waves. The static corrections are done to compensate the effects of the weathering zone. In the example, the 3D static corrections are very weak.

The data are sorted in Common Mid-Point gathers (CMP). Normal Move Out (NMO) corrections are done with a stacking velocity model obtained by velocity analysis. Surface consistent residual statics are computed to enhance the signal to noise ratio and preserve the high resolution of the data in the CMP stack procedure.

The 3D block is composed of 13 in-line sections 1 m apart. Each section is composed of 44 CMP points 1 m apart. Figure 2.29 shows an example of in-line and crossline seismic sections extracted from the 3D block. The two sections presented (section 6 in the in-line direction, and section 23 in the crossline direction) intersect in the middle of the 3D block. They have been filtered in the 15-100 Hz bandwidth, which provides an excellent signal-to-noise ratio.

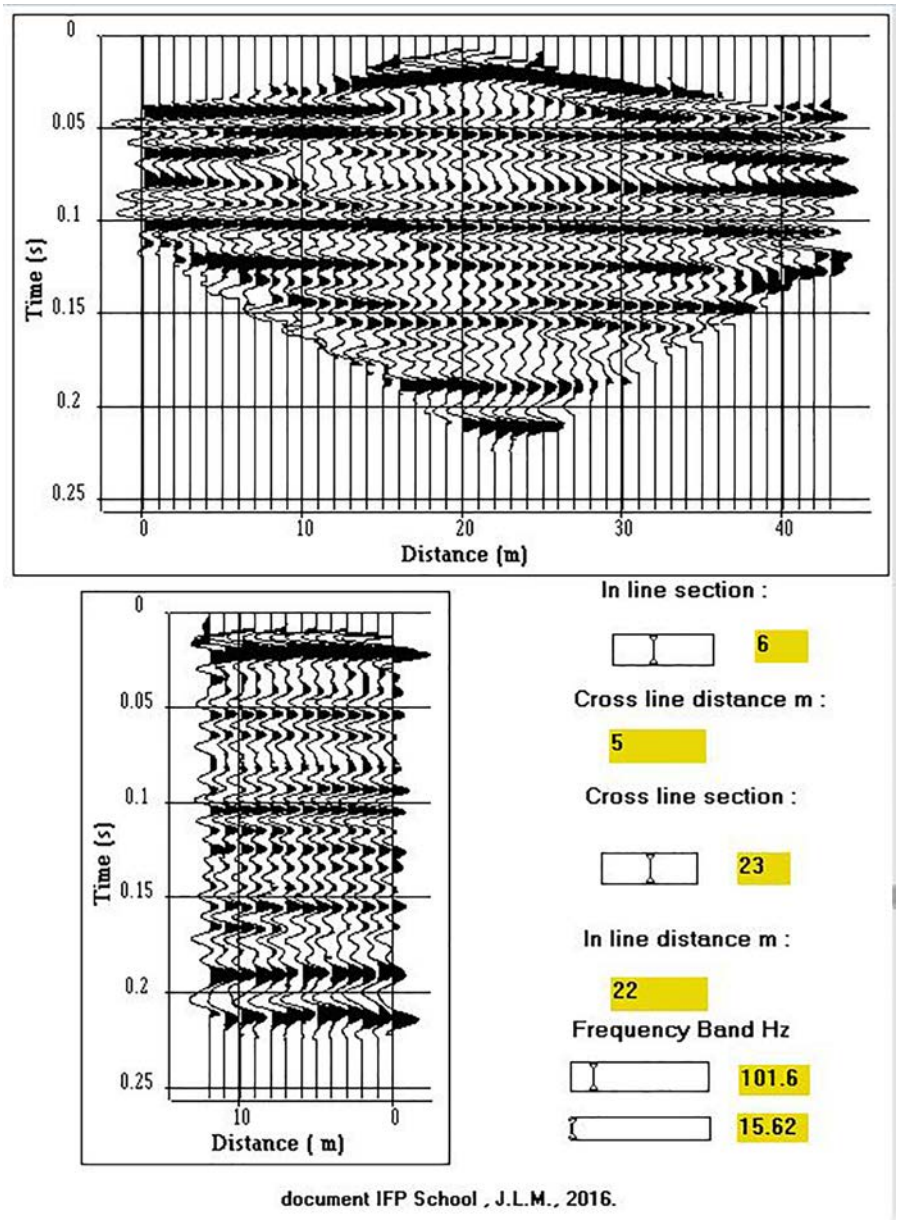


Figure 2.29 *CMP stacked sections. The high-resolution 3D cube has revealed near surface seismic horizons between 50 and 200 ms. After Mari and Mendes (2019).*

The safety of the Callovo-Oxfordian argillaceous rock (Cox) storage in the eastern Paris Basin is the major concern of the French National Radioactive Waste Management Agency (Andra). Extensive research on the clay sealing and healing properties as well as on the best way to characterize them on site have been conducted for over 20 years now. High resolution 3D seismic data have been acquired on a 30km2 underground zone, known as a zone of interest for in-depth reconnaissance (ZIRA), in the vicinity of 3 exploration drillholes. Figure 2.30a shows a view of the geological model of the site and the location map of the 3D seismic survey. The seismic processing sequence is basically a pre stack time migration and an elastic inversion of the 3D block in time (Mari and Yven, 2019). Figures 2.30b to 2.30d shows the PSTM section, the Ip and Is impedance sections obtained for the in-line IL405.

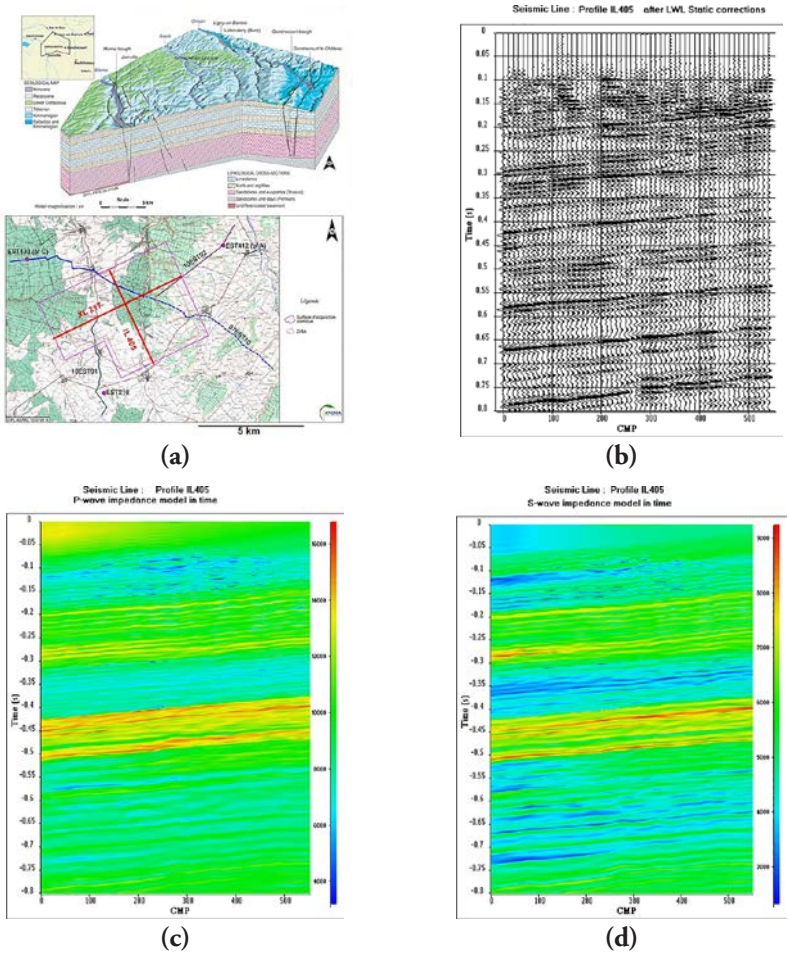


Figure 2.30 *3D pre stack time migration and elastic inversion of the IL 405 profile. (a) Geological model and location map of the 3D survey, (b) PSTM sections, (c) Ip section, (d) Is section. After Mari and Yven (2019), (Andra document).*

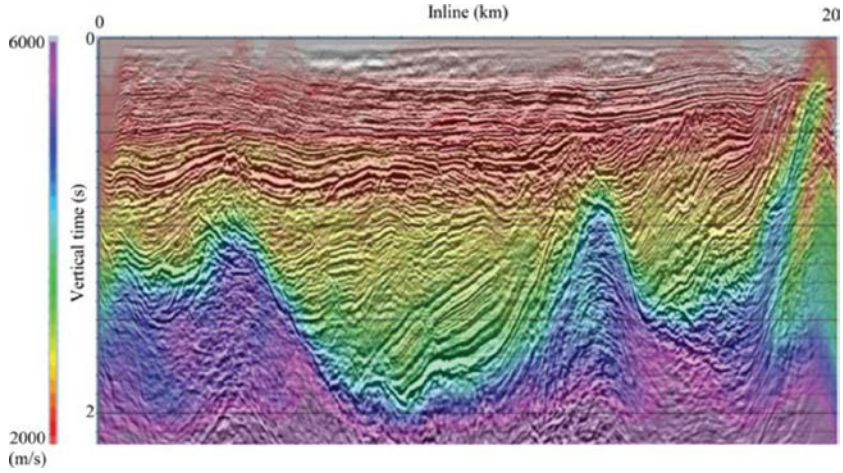


Figure 2.31 *Migrated section superimposed on the FWI velocity model, in a land example (Baeten et al., 2013).*

Full Waveform Inversion (FWI; Chauris, 2019) is a processing technique to derive quantitative images of the subsurface from seismic measurements. By quantitative, we mean for example P-wave velocity models expressed in m/s, and not only a structural image of the Earth as a classical stack section would provide. The principle is simple: the optimal model is the one for which the computed shot gathers are reproducing the observed shot data. More details on the formulation are provided in the literature (Louboutin et al., 2017, 2018). Beyond the apparent simplicity, the practical applicability of FWI is a difficult task. This is a non-linear process; the user should provide an initial model; the quality of the final inverted model depends on the reliability of the low frequency content of the observed data. A proper strategy should be established to iteratively determine the model (typically by successively introducing higher frequencies). One also needs to use the adequate wave equation to generate synthetic wave fields and associated shot gathers to mimic the physics of wave propagation. Finally, due to the limited data frequency band and limited data acquisition from the surface only, FWI does not necessarily lead to a unique solution. For example, if the user is interested in determining P-velocity and density models, there is an intrinsic trade-off between the two quantities, especially for short offset data. This is not specific to FWI: other imaging techniques suffer from the same effect, but this is visible in the FWI context as FWI is expected to provide quantitative results. Many FWI results have been published on real data in seismology, as well as at the exploration scales, at least in the marine case. The use of the technique on land with onshore data, however, has only been proven for a limited number of applications due to the presence of strongly energetic surface waves.

The example shown in Figure 2.31, in a land acquisition context (Inner Mongolia, China), is challenging due to the presence of highly energetic surface waves (Baeten et al., 2013; Brossier et al., 2009). Here, surface waves are filtered out in

a pre-processing step. The initial velocity is derived from travel time tomography and is mainly a 1D model (not represented here). Specific attention is paid to the preservation of energy in the dataset between 1.5 to 2 Hz: this is a crucial step in the FWI construction of the velocity model.

Acoustic FWI largely outperforms standard travel time tomography. More work is needed in future to consider higher frequencies and more complex physics.

The obtention of accurate velocity models is a key point for seismic imaging and for estimating mechanical and petrophysical properties of geological formations. Velocity models can be obtained by tomography, full waveform inversion or simultaneous joint inversion of seismic and non-seismic measurements (De Stefano et al., 2021). Simultaneous joint inversion of two sets of geophysical data (seismic and ERT) can lead to obtaining two consistent geophysical models (seismic velocity and resistivity) to characterize geological heterogeneities (Gallardo and Meju, 2004). Ceci et al. (2024a,b) shows an example of application of an integrated Multiphysics modelling workflow, including 3D MT, 2D seismic and 3D gravity data where the combined use of the data allows the reduction of the intrinsic uncertainty of each method and the obtention of a consistent seismic velocity field controlled by MT and gravity measurements.

Geothermal reservoirs can be explored and characterized using reflection seismic methods. The use of seismic methods remains a challenge for geothermal exploration due to a lack of reliable well and seismic data stemming from limited budgets and access restrictions when operating in urbanized areas.

Through the last few years, porosity and permeability in the Dogger and in the Triassic reservoirs of Paris basin have been a big challenge depending on their location, particularly under tertiary deposits. Nowadays, predicting the reservoir quality from seismic is one of current challenge to derisk the geothermal topics, west of Paris Basin, near to the "Sillon marneux" area. For decades, this subject has been a real challenge, as a dedicated 3D seismic survey was shot in the Villeperdue area in 90's to study the capacity of seismic to highlight reservoir quality variations. The approach needs to strongly correlate well and seismic data. Because of the distance between wells with interesting information, the use of seismic needs to integrate several seismic lines. CDP Consulting developed through these past years several programs of regional lines combining old vintage lines to recognize an overall basin.

In this way, an innovative sequence must be developed to highlight the favourable reservoir areas, for many topics, particularly for geothermal derisking. This integrates an accurate 2D seismic sequence, possibility to provide seismic inversion on true amplitude PSTM.

To perform accurate reservoir study from seismic line, it is very important to avoid some key points:

- avoid seismic artefact, particularly due to stack optimization (problem of statics and signal to noise ratio),
- avoid effects linked to the change of seismic parameters between lines from different seismic campaigns and introducing several difficulties in many steps of processing.

For seismic onshore data, and particularly in the centre part of Paris basin (mainly on Tertiary cover in the Ile de France), the quality of the seismic processing is particularly dependent on static corrections.

The Tertiary units have a thickness never exceeding 250 m. But the wide variability of seismic units (limestones, marls, evaporites, sands, clays) make the velocity variations very strong and dependant on the different aquifers. Many velocity inversions make totally forbidden the use of refraction statics to compute primary statics. Indeed, such use of refraction statics is totally unsuitable in this area and provides wrong structural shapes, cycle skips and loose of signal noise ratio. Such wrong artefact caused by refraction statics have induced in the past very strong artefacts and misunderstanding in reservoir characterization. They also lead in the past to drill a lot of wrong structures in time that have no reality in depth and cause the main failure of the oil and gas exploration in Paris Basin.

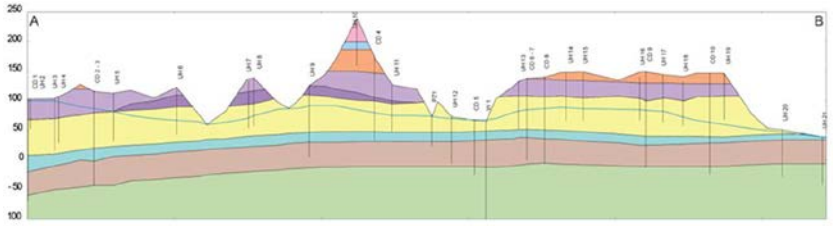


**(a)**

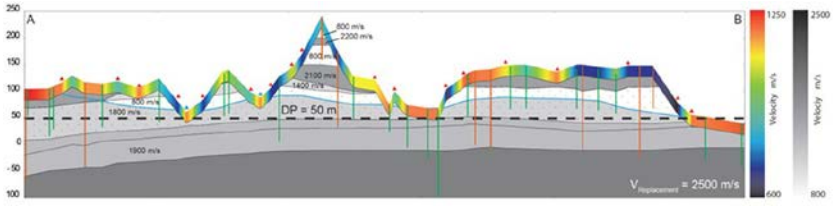


**(b)**

Figure 2.32 *Example of geological modelling for static computation based on geological data (up holes). (a) Geological model, (b) geological velocity model (CDP Consulting document).*

The only way to optimize the stack quality and get confidence in final seismic data needs to follow an accurate processing sequence. This needs to integrate a modelling of primary statics supported by a well constrained geological velocity model of the Tertiary units. CDP Consulting has developed a dedicated methodology for primary static computation based on Franck Hanot experience and widely discussed in many publications (Hanot, 1992; Hanot et al. 2012; Miquelis et al., 2016, 2019; Nosjean et al, 2017). Consequently, the pitfalls induced by static problem can be solved and need to be integrated in derisking of geothermal exploration (depth/temperature well design and reservoir characterization).

Figure 2.32 is an example of geological modelling for static computation based on geological data (up holes). The methodology is particularly efficient when the merge of seismic data with different parameters is strong, and when the quality of refraction is very poor as in Fontainebleau sands area or noisy locations in densely populated areas. A particular attention must be also to tackle the noise effect depending on the location and phenomena of signal absorption due to thick deposit of dry sands (west part of Paris basin). Figure 2.33 shows the effects of static corrections on a vintage line of a seismic campaign "Paris Ile de France" (1986). Figure 2.33a shows the line processed with conventional refraction static corrections (paragraph 2.4.1) and highlights the strong difficulty to stack below the Fontainebleau sands (central part of the figure). Figure 2.33b shows the same line processed with the CDP Consulting methodology for the primary statics. One can notice a good continuity of the seismic horizons below the Fontainebleau sands, sustaining a good reservoir quality approach.

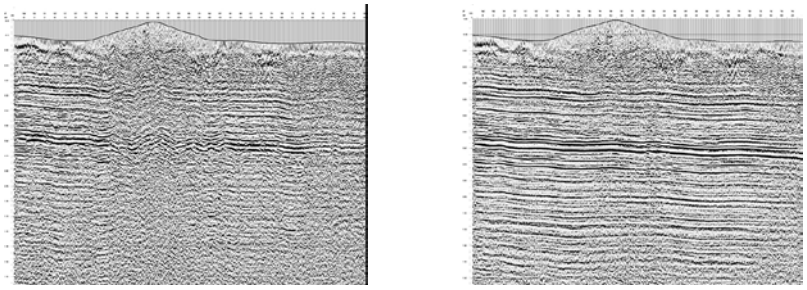

**(a)** **(b)**

Figure 2.33 *Effect of static corrections on the seismic stack (CDP Consulting document). (a) Conventional static method, (b) CDP Consulting method.*

In Paris Basin, static problems due to the chalk diagenesis, already described in 1961 by Millouet, is superposing to the static problems induced by tertiary deposits. In the same way than the tertiary deposits, the chalk effects could lead to strong artefacts of dogger reservoir imagery. The problems are particularly difficult to master because they are very often wider than the seismic line. The chalk problem needs to be accurately considered for geothermal exploration in sensitive place of Paris Basin, particularly under tertiary deposits (Hanot et al., 2012; Miquelis et al., 2016).

After having solved individual static problem and stack quality of individual line, producing regional line in true amplitude processing needs to follow a very detailed specific sequence including homogenous static modelling over the whole area, and a very specific approach in terms of geometry, noise removal, velocity picking and migration parameter. Once this very specific workflow is successful, extended regional lines could be used for the seismic reservoir quality quantification, notably for geothermal energy.

Figure 2.34 is an example of a regional line of more than 100 km in true amplitude PSTM processing composed of 12 vintage lines belonging to 8 seismic campaigns with different parameters (sweep, number of vibrators, distance between shots, distance between seismic traces, geophone filtering, etc.).

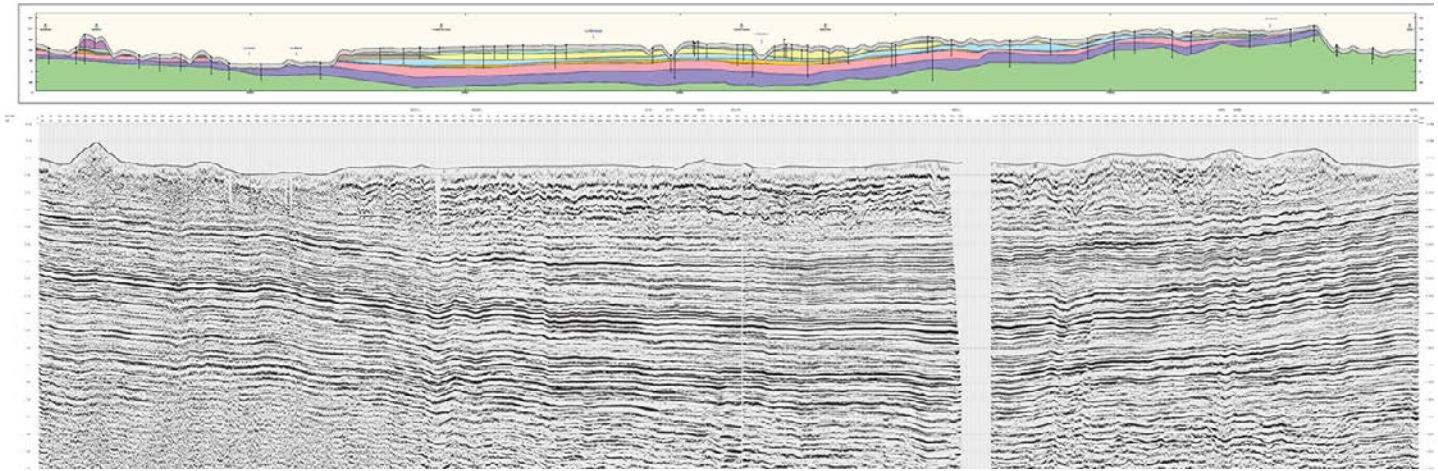

Figure 2.34 *Example of regional line (CDP Consulting document).The line is composed by the merge of 12 individual seismic line belonging to 8 different seismic campaigns and resulting in a homogenous Prestack time Migration stack section in true amplitude processing, and that could be then integrated in an advanced reservoir quantification approach allowed by the numerous wells crossing this line. The regional line is here superposed to the geological model of Tertiary deposits used for static corrections.*

The recent development of advanced deep neural networks (DNNs) has opened the door to a new viable approach for directly estimating reservoir properties from seismic data (Formento et al., 2021). Although this kind of neural network requires a large amount of labelled data to be trained, only a limited amount of real well data is required as synthetic data can be used to augment the training set. Recently introduced theory-guided techniques based on rock physics models can help generate a large training set of pseudo-logs, representative of geologic variations, used to feed the DNN for a prediction of petrophysical properties of geological formations from full stack seismic profiles (Formento et al., 2021).

The methodology was successfully applied to improve the understanding of the potential for deep geothermal energy in the south of the Paris Basin (Souvannavong et al., 2024). The available seismic data are limited to 600 km of old 2D lines acquired between 1970 and 1990 and 10 old wells which had an available set of Caliper, Gamma Ray (GR), compressional sonic (DTP), density (RHOB), neutron (NPHI) and resistivity logs. The old seismic lines were reprocessed. More than 800 pseudo wells were generated to account for possible geological changes within the 3 reservoir units (Oxfordian, Dogger and Trias), allowing to have a large training set to feed the deep neural network, for a better prediction of total porosity (PHIT) and volume of clays (VCL) from full stack seismic. Figure 2.35a shows a seismic line passing through one of the wells with color-coded reservoir intervals (blue for Oxfordian, purple for Dogger and red for Trias). The estimated PHIT and VCL sections are shown in Figures 2.35b and 2.35c. Figure 2.35d shows the match between the recorded and synthetic seismic traces. On this figure, from left to right: the AI log is displayed in grey to show the acoustic contrast between layers. Then the comparison between the synthetic (black) and recorded seismic trace (red) shows a satisfactory match within the Oxfordian and Dogger intervals but a relatively poor one for the Trias where seismic signal-to-noise ratio (S/N) is lower. Figure 2.35e shows the match between the estimated attributes and the well logs. The predicted attributes (red traces) match well to the log data in general. In the Oxfordian interval, the predicted porosity correctly captures the layer with high porosity at the top of the reservoir (blue arrow on Figure 2.35e). This study illustrates how rock physics-guided deep neural networks were used as a practical alternative to derive accurate total porosity and volume of clay attributes for two carbonate reservoirs (Oxfordian and Dogger) and a clastic reservoir (Trias) directly from full-stack seismic and limited well data (Souvannavong et al., 2024).

Reinsch et al. (2017) demonstrated that temperature influences seismic velocities significantly. Du et al. (2024) have studied the Influence of temperature on the velocity-porosity relationship, with laboratory measurements on geothermal core samples. Laboratory measurements have shown that P-wave velocity continually decreases with increasing temperature. This trend in seismic velocity with temperatures is related to microfractures. Using the temperature-dependent Kuster-Toksöz equation (Kuster, 1974), it is suggested that the presence of fluid and microfractures can reduce the effective elastic properties of rocks (Du et al., 2024).

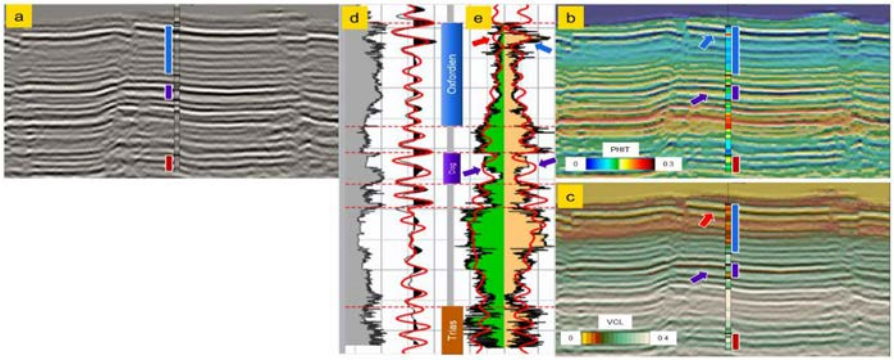


Figure 2.35 *DNN results: (a) seismic section with well synthetic; (d) 1D QC at well location showing from left to right AI log (grey), well synthetic (black), seismic (red); (e) 1D QC at well location showing VCL log (green), PHIT log (orange) and corresponding inferred PHIT and VCL (red); (b) PHIT section and log; (c) VCL section and log (after Souvannavong et al., 2024).*

By adopting the thermoacoustic wave equation, Yang et al. (2024) have proposed a full-waveform inversion method to directly invert temperature and velocity parameters using seismic data. The method has been checked on synthetic data sets. Figure 2.36 shows the exact or real velocity and temperature models, composed of 301 traces over 3 km (a trace every 10 m). Figure 2.37 shows the a priori or initial velocity and temperature models used as input data for the inversion process. Figure 2.38 shows the inversion results both for the complete models and for the trace 135, situated at the abscissa 1.35 km. The results are promising (comparison of inversion results with real models at trace 135). Further developments may enhance the method's applicability and accuracy in geothermal reservoir assessment (Yang et al., 2024).

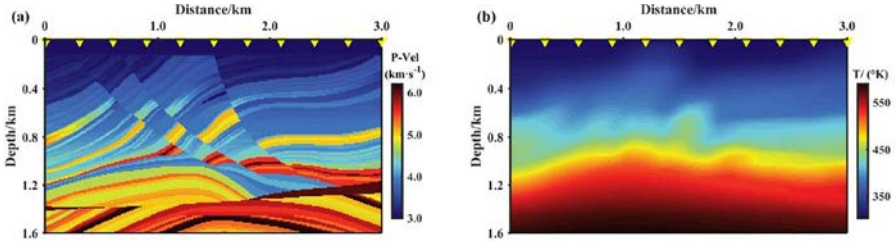


Figure 2.36 *Velocity and temperature full waveform inversion (after Yang et al., 2024). Real models: velocity (a) and temperature (b).*

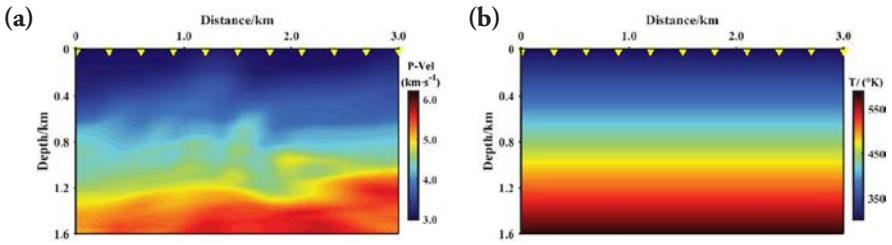


Figure 2.37 *Velocity and temperature full waveform inversion (after Yang et al., 2024). Initial models: velocity (a) and temperature (b).*

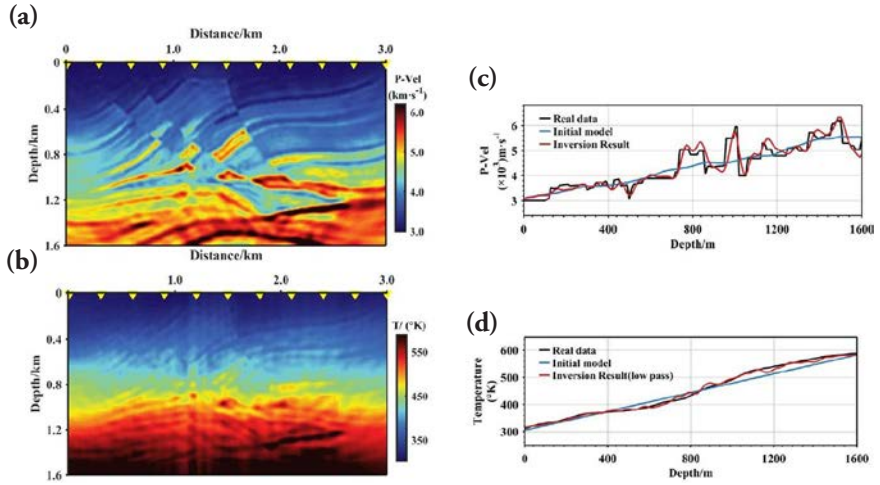


Figure 2.38 *Velocity and temperature full waveform inversion (after Yang et al., 2024). Inversion results: velocity model (a) and temperature model (b), velocity at trace 135 (c) and temperature at trace 135 (d).*

## Passive seismic method and MASW method

In addition to body waves (P- and S-waves) which propagate within the subsurface, a surface seismic source generates surface waves (Love and pseudo-Rayleigh waves). The seismic method based on the analysis of surface waves is called MASW (Multiple Analysis of Surface Waves). Surface waves, which are mainly sensitive to the shear modulus of the formation, propagate through the earth with their energy concentrated near to the surface. Their propagation velocity is frequency-dependent (dispersion). The degree of dispersion is a measure of seismic wave velocity as a function of depth and can be used to calculate the thickness of surface layers. Travelling only within a few seismic wavelengths from the surface of a solid, the lower the frequency of a surface wave, the deeper its penetration depth into the earth. Therefore, in the same medium, waves of different wavelengths affect different depths.

The processing classically applied to surface waves is based on spectral analysis and involves two steps. The first step is the construction of a dispersion curve (a plot of phase-velocity against frequency). The next step aims to obtain shear wave velocity (i.e. stiffness) profiles as a function of depth and horizontal position along the seismic survey line. The profiles are calculated using one of the two iterative purposes: matching the experimental dispersion curves to a theoretical curve derived from forward analytical modeling (usually 1D model) or an automatic least-squares approach.

A geophysical survey was carried out in Yellowstone National Park (USA), in the Obsidian Pool Thermal Area. The goal of the seismic survey carried out at this site was to study shallow hydrothermal systems, characterize fluid pathways and improve understanding of the depths at which steam separates from liquid water. The area is characterized by extensive $CO_2$ diffuse degassing and isolated thermal features with water temperatures between 21.9 and 84.0 °C. Seismic data were collected in July 2016 along a south-southwest–north-northeast transect, crossing a heat-flow anomaly between 50 and 120 m and a degassing feature between 86 and 96 m.

The equipment and parameters used in the seismic survey were:

- a 5.4 kg sledgehammer source swung onto a metal plate. The plate was hit five times at each position to increase the S/N,
- 10 Geometrics Geode seismographs, with 24-channels in each one,
- 4.5 Hz vertical component geophones spaced every 1 m, obtaining a 239 m long profile,
- 25 shot gathers recorded every 10 m,
- a sampling rate of 0.125 ms and a recording time of 0.75 s, to include the full surface wavefield.

In addition, a GPS survey and airborne LiDAR data collection were carried out to extract the topography.

The processing of the surface waves data was carried out using SWIP and readers can find supplementary information about this practical processing sequence in Pasquet and Bodet (2017).

After field data windowing for validation of the 1D model hypothesis, the seismic record from its original time–distance domain was transformed into the frequency–phase-velocity domain. This step results in a set of frequency–phase-velocity pairs specifying dispersion curves. The experimental dispersion curves were identified in the f-k domain and the location of maxima energy were picked. The dispersion curve is a diagram of phase velocity versus frequency and Figure 2.39 (Top) shows examples of single dispersion curves from shots located at 0 m, 10 m, 50 m, and 60 m. Through the utilization of multi-shot acquisition setups, the inversion of the sets of dispersion curves leads to Pseudo-2D section of average S-wave velocity model (Figure 2.39, bottom) The S-wave velocity model is characterized by velocities ranging between 50 and 600 m/s, with higher shallow velocity below the heat-flow anomaly observed between 50 and 120 m.

Passive seismic can be implemented for MASW. Passive seismic tomography or interferometry is a technique used to explore (image and monitor) the subsurface using ambient noise generated by natural or anthropogenic sources (Shapiro et al., 2005; Gouedard et al., 2008; Mordred et al., 2013).

Interferometry is based on calculating cross-correlations of the noise signal between pairs of seismic sensors. The noise is dominated by surface waves propagating in the shallow subsurface (Roux et al., 2011; Shapiro and Campillo, 2004). The calculation of cross-correlation between pair of sensors allows the extraction of the surface wave contained in the noise propagating between the sensors. As for MASW, dispersion curves of surface waves are computed and inverted to obtain distribution of S-wave velocity in the subsurface. In practice, several tens of sensors (vertical geophones) are deployed on the ground surface, the listening time can be of several hours or days, the analysis of the dispersion of surface waves is done in the low frequency domain (5–20 Hz).

Figure 2.40 shows an example of 3D shear velocity model obtained by passive seismic tomography, implemented for 3D imaging of the subsurface in a tunnel area (Saade et al., 2024). For the study, 199 surface sensors are used, covering the study area with a variable inter-sensor distance averaging about 20 m, and approximately 336 hours of measurements were recorded.

Passive seismic interferometry can be used for the monitoring of subsurface fluids – from shallow groundwater to native or storage gas reservoirs (Kremer et al., 2024)

Seismic interferometry has been used to investigate velocity variations, and subsequently strain sensitivities, related to a seismic swarm activity that occurred in 2013 along the Alto Tiberina low angle normal fault (Mikhael et al., 2024). Through an optimization procedure based on synthetic modeling to separate the non-tectonic from the tectonic induced velocity variations, a significant velocity variation in response to small strain perturbations has been unraveled. The deduced strain sensitivity value is comparable to values observed in volcanic settings suggesting the presence of pressurized fluids at depth (Mikhael, 2024). The same approach could be applied in similar contexts where fluids are involved including the monitoring of geothermal systems.

In the Eastern Vienna array, a seismic ambient noise survey was conducted for geothermal exploration (Esteve et al., 2024). A reservoir-scale 3-D shear velocity model of the central Vienna basin was obtained by passive seismic interferometry using recordings of ambient seismic noise. 100 seismic nodes were deployed for a duration of 6 weeks during the summer 2023. It has been shown that the location of the Markgrafneuseidl fault is highlighted by a strong velocity contrast in the 2D Love wave group-velocity maps at periods shorter than 3s. The 3D shear-wave velocity model shows a basin shape structure, which is interpreted to be the seismic signature of the Schwechat depression, the main target for geothermal exploration in Vienna (Esteve et al., 2024). Ambient Noise Tomography can support the growth of geothermal sector by providing reliable and affordable exploration methods. This can improve understanding of the subsurface and help reduce drilling uncertainty (Esteve et al., 2024).

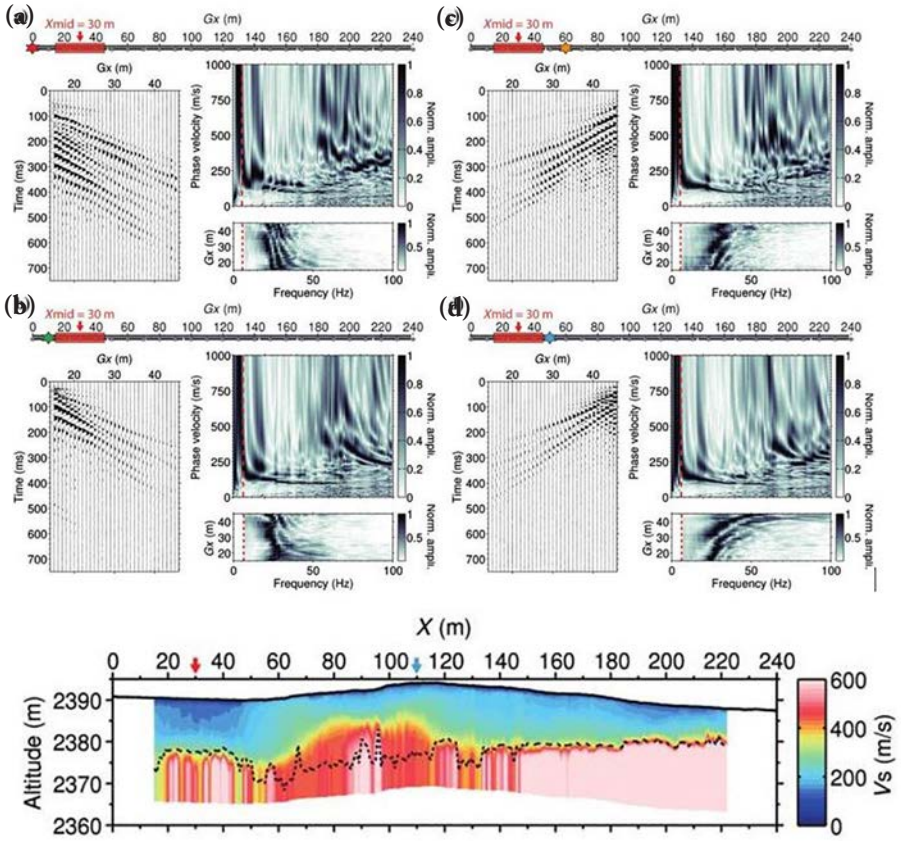


Figure 2.39 *Example of MASW (after Pasquet and Bodet, 2017). Top: Extraction of single dispersion images for a 31-trace window centered at $X_{mid}$ = 30 m, using shots located at (a) 0 m, (b) 10 m, (c) 50 m, and (d) 60 m. On each inset, windowed shot gathers are on the left, corresponding spectrograms are at the bottom right, and computed dispersion images are at the top right. The dashed red lines on the spectrograms and dispersion images correspond to automatic low-cut frequencies defined from the spectrogram amplitude. Bottom: pseudo-2D section of average S-wave velocity model computed from accepted models at each $X_{mid}$ position along the line. The dashed black line corresponds to the depth of investigation estimated with an S-wave velocity model standard deviation threshold of 150 m/s. The topography extracted from airborne LiDAR data is represented with a solid black line.*

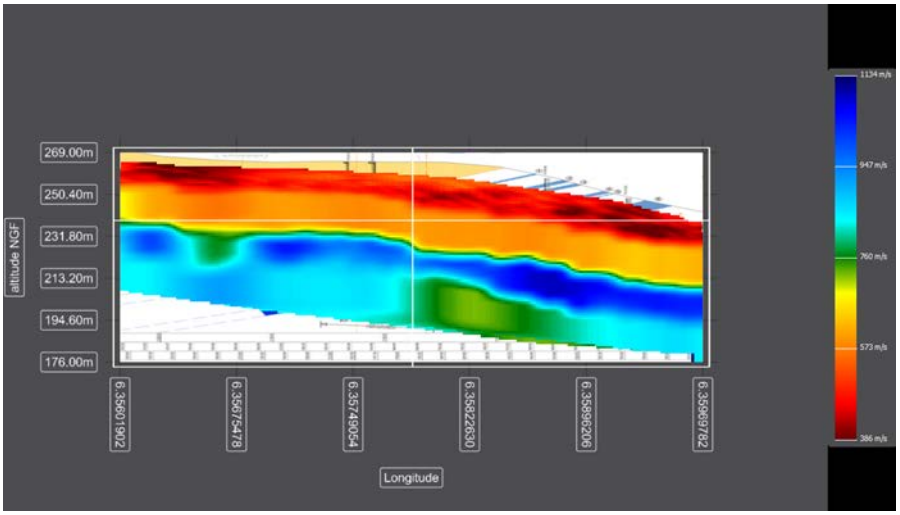


Figure 2.40 *3D shear velocity model obtained with surface data (Saade et al., 2024).*

## Conclusion

In conclusion, we have introduced the physical properties of rocks and pore spaces, followed by a review of geophysical methods and their field applications, notably for geothermal energy. These methods play a crucial role in building 2D or 3D subsurface models:

- gravity and gravity-gradiometry are sensitive to density variations,
- magnetic methods respond to rock magnetization properties, including magnetic susceptibility and remanence,
- electrical and electromagnetic (EM) methods capture resistivity variations,
- seismic methods are influenced by both velocity and density variations.

The selection of a geophysical method must be guided by the specific contrasts in petrophysical properties best suited to detecting the desired anomalies. Additionally, acquisition parameters need to be carefully chosen to target the appropriate depth, and both vertical and horizontal resolutions must be evaluated to ensure the method's suitability for identifying anomalies of a given size.

In many cases, combining multiple geophysical methods can improve the recovery of several physical rock properties simultaneously or enhance the capabilities of one method through the complementary strengths of another. For instance, the resolution of EM methods can be significantly enhanced through the integration of seismic methods (Alvarez et al., 2017).

Processing these data often involves simultaneous or joint inversion techniques, such as:

- refraction tomography combined with electrical resistivity tomography (ERT),
- acoustic impedance inversion paired with controlled-source EM (CSEM), magnetotelluric (MT), or deep ERT.

In near-surface studies, multiple methods can be used together to produce a more detailed geological model. For example, combining P-wave refraction tomography with MASW provides both P-wave and S-wave distributions, allowing for the computation of mechanical parameters such as Poisson's ratio (Pasquet and Bodet, 2017).

For deeper targets, seismic reflection methods, which provide both structural and petrophysical information about a reservoir, can be combined with CSEM to detect the presence of hydrocarbons (Alvarez et al., 2017). However, it is essential to calibrate surface geophysical results with borehole measurements, including well log and borehole seismic data.

Passive methods, being less invasive and cost-effective, are valuable tools. When combined, passive seismic, MT, and gradiometry can yield a shear velocity model, resistivity distribution with depth, and insights into bedrock location and fault structures. Passive techniques can also identify specific areas for more detailed active seismic surveys and extend coverage where conventional seismic methods are impractical.

Overall, the integration of multiple geophysical methods enhances subsurface imaging and offers more reliable insights, enabling more informed decision-making in geological exploration and reservoir characterization.

## References

*The writing of the chapter (text and relative figures) is mainly based on the following papers and books.*

Achenbach J.D. (1973) *Wave propagation in Elastic solid*, North Holland Publishing Company, 3rd Ed.

Alvarez P., Alvarez A., MacGregor L., Bolivar F., Keirstead R., Martin T. (2017) Reservoir properties prediction using controlled-source electromagnetic, prestack seismic, and well-log data: Case study in the Hoop Area, Barents Sea, Norway, *Interpretation* 5(2), 1-17, https://doi.org/10.1190/INT-2016-0097.1.

Archie G.E. (1942) The electrical resistivity log as an aid in determining some reservoir characteristics, *Petroleum Technology* 1, 55-67.

Avram Y. (2017) MT for onshore oil discovery, from e-book devoted to electromagnetic methods in geophysics (http://books.ifpenergiesnouvelles.fr/ebooks/ifpen-electro/).

Baeten G., De Maag J.W., Plessix R.-E., Klaassen R., Qureshi T, Kleemeyer M., Ten Kroode F., Rujie Z. (2013) The use of low frequencies in a full-waveform inversion and impedance inversion land seismic case study, *Geophysical Prospecting* 61(4), 701-711, https://doi.org/10.1111/1365-2478.12010.

Bell R.E, Anderson R., Pratson L. (1997) Gravity gradiometry resurfaces, *The Leading Edge* 16, 55-59.

Bourbiaux B., Callot J.P., Doligez B., Fleury M., Gaumet F., Guiton M., Lenormand R., Mari J.L., Pourpak H. (2007) Multi-Scale Characterization of a Heterogeneous Aquifer Through the Integration of Geological, Geophysical and Flow Data: A Case Study, *Oil and Gas Science and Technology, Rev. IFP* 62, 347-373.

Brossier R., Operto S., Virieux J. (2009) Seismic imaging of complex on-shore structures by 2D elastic frequency-domain full-waveform inversion, *Geophysics* 74, WCC105–WCC118, https://doi.org/10.1190/1.3215771.

Carrier A., Fischanger F., Gance J., Cocchiararo, Morelli G., Lupi M. (2019) Deep electrical resistivity tomography for the prospection of low – to medium – enthalpy geothermal resources, *Geophys. J. Int* 219, 2056-2072.

Ceci F., Clementi M., De Luca L., Marin M., Wojdyla M, Sito Ł., McConvey P., Raine R., Clements S. (2024a) Multiphysics data acquisition and modelling in a highly urbanized area: a case study from Northern Ireland, 5th Global Energy Transition Conference & Exhibition, Rotterdam, Nederland.

Ceci F., De Luca L., Sirtori A., Olaiz A., Garcia I., Torre J., Garcia A., Marro G., Ambrogio A. (2024b) Geothermal potential assessment via Multiphysics modelling: a case study from Gran Canaria, 5th Global Energy Transition Conference & Exhibition, Rotterdam, Nederland.

Chaouch A., Mari J.L. (2006) 3-D land seismic surveys: Definition of Geophysical parameters, *Oil & Gas Science and Technology, Rev. IFP* 61(5), 611-630, https://doi.org/10.2516/ogst:2006002.

Chapellier D. (2001a) Basic principles course, from On-line course of geophysics (http://www-ig.unil.ch/).

Chapellier D. (2001b) Electrical methods, from On-line course of geophysics (http://www-ig.unil.ch/).

Chauris H. (2019) "Full waveform inversion", Chapter 5 in *Seismic imaging: a practical approach*, EDP Sciences, https://www.edp-open.org/seismic-imaging-a-practical-approach.

Constable S., Parker R., Constable C. (1987) Occam's inversion: A practical algorithm for generating smooth models from electromagnetic sounding data, *Geophysics* 52, 289-300.

Cordsen A., Galbraith M., Peirce J. (2000) Planning land 3-D seismic surveys – SEG Series n° 9, Bob A. Hardage Ed.

De Stefano M., Golfre' Andreasi F., Re S., Virgilio M., Snyder F.F. (2011) Multiple-domain, simultaneous joint inversion of geophysical data with application to subsalt imaging, *Geophysics* 76(3), R69-R80.

Dobrin M.B., Savit C.H. (1988) *Introduction to Geophysical Prospecting*, 4th edition McGraw-Hill Book Co. 867 p.

Du Q., Yasin Q., Sohail G.M., Majdanski M. (2024) A Study of the Influence of Temperature on the Velocity-Porosity Relationship in Geothermal Core Samples, 85th EAGE Annual Conference & Exhibition, Oslo, Norway.

Esteve C., Lu Y., Bokelmann G., Gosselin J. (2024) Seismic ambient noise tomography for geothermal exploration: the Eastern Vienna Array, paper 1124, 85 th EAGE Annual Conference & Exhibition, Oslo, Norway.

Fabricius I.L., Baechle G., Eberli G.P., Weger R. (2007) Estimating permeability of carbonate rocks from porosity and Vp/Vs, *Geophysics* 72(5), 185-191, https://doi.org/10.1190/1.2756081.

Fairhead J.D. (2015) *Advances in gravity and magnetic processing and interpretation*, EAGE publications, ISBN 978-94-6282-175-0.

Faust L.Y. (1953) A velocity function including lithologic variation, *Geophysics* 18, 271-288.

Formento J.L., Allo F., Coulon J.P., Reboul R., Capar L., Darnet M., Marc S., Issautier B., Stopin A. (2021) Unlocking geothermal reservoir seismic characterization with physics-guided deep neural networks, *2nd EAGE Conference on Global Energy Transition*, Extended Abstracts.

Galbraith M. (2000) 3D seismic survey design: a solution, *First break* 18(5), 171-176.

Gallardo L.A., Meju M.A. (2004) Joint two-dimensional DC resistivity and seismic travel time inversion with cross gradient constraints, *J. Geophysical Research Atmosphere* 109, B03311, https://doi.org/10.1029/2003JB002716.

Girard J.F. (2017) MT for geothermal exploration, from e-book devoted to electromagnetic methods in geophysics, http://books.ifpenergiesnouvelles.fr/ebooks/ifpen-electro/.

Gouedard P., et al. (2008) Cross-correlation of random fields: mathematical approach and applications, *Geophys. Prospect*, 56(3), 375-393.

Hagedoorn G.J. (1959) The Plus–Minus method of interpreting seismic refraction sections, *Geophysical Prospecting* 7, 158-182.

Hanot F. (1992) Seismic applications of a Paris Basin shallow geology database, *First Break* 10(5), 175-188.

Hanot F., Vicelli J., Miquelis F., Oliviero G. (2012) Diagenèse de la craie du bassin parisien. Hypothèse d'un biseau salé d'âge éocène. Couplage des données industrielles et géologiques, *Bulletin d'information Géologique du Bassin de Paris* 49(2), 6-24.

Key K. (2016) A 2-D inversion code for controlled-source electromagnetic and magnetotelluric data, *Geophysical Journal International* 207, 571-588.

Kozeny J. (1927) Über kapilläre Leitung des Wassers im Boden, *Sitzungsberichte der Wiener Akademie der Wissenschaften* 136, 271-306.

Kremer T., Voisin C., Gaubert-Bastide T., Ars J.M., Mouquet P., Moinet F., Ferran J.C. (2024) The use of passive seismic interferometry for the monitoring of subsurface fluids – from shallow groundwater to native or storage gas reservoirs, Journees Scientifiques AGAP 2024, EDP Sciences, https://doi.org/10.1051/e3sconf/202450402003.

Kuster G.T. (1974) Velocity and Attenuation of Seismic Waves in Two-Phase Media: Part I. Theoretical Formulations, *Geophysics* 39, 587.

Lansley M. (2000) 3D seismic survey design: a solution, *First break* 18(5), 162-166.

Lavergne M. (1986) *Seismic Methods*, Editions Technip, Paris.

Louboutin M., Witte P., Lange M., Kukreja N., Luporini F., Gorman G., Herrmann F.J. (2017) Full-waveform inversion, Part 1: Forward modelling, *The Leading Edge* 36(12), 1033-1036, https://doi.org/10.1190/tle36121033.1.

Louboutin M., Witte P., Lange M., Kukreja N., Luporini F., Gorman G., Herrmann F.J. (2018) Full-waveform inversion, Part 2: Adjoint modeling, *The Leading Edge* 37(1), 69–72, https://doi.org/10.1190/tle37010069.1.

Mari J.L. (2011) *Signal processing for geologists and geophysicists*, IFP Energies Nouvelles ebook, http://books.ifpenergiesnouvelles.fr/ebooks/signal-processing/.

Mari J.L, Guillemot D. (2012) Detection of porous and permeable formations: from laboratory measurements to seismic measurements, *Oil & Gas Science and Technology Rev. IFP Energies nouvelles* 64(4), 703-721, https://doi.org/10.2516/ogst/2012009.

Mari J.L., Mendes M. (2012) High resolution 3D near surface imaging of fracture corridors and cavities by combining Plus-Minus method and refraction tomography, *Near Surface Geophysics* 10, https://doi.org/10.3997/1873-0604.2011052.

Mari J.L., Mendes M. (2019) *Seismic imaging: a practical approach*, EDP Sciences, https://www.edp-open.org/seismic-imaging-a-practical-approach.

Mari J.L., Vergniault C. (2018) *Well seismic surveying and acoustic logging*, EDP Sciences, https://www.edp-open.org/well-seismic-surveying-and-acoustic-logging.

Mari J.L., Yven B. (2019), "Integrated seismic study", Chapter 7 in *Seismic imaging: a practical approach,* EDP Sciences, https://www.edp-open.org/images/stories/books/contents/SeismicImaging/SeismicImaging_10.1051_978-2-7598-2351-2.c009.pdf.

Mari J.L., Glangeaud F., Coppens F. (1997) *Signal processing for geologists and geophysicists*, Technip Ed., Paris.

Mari J.L., Peignard L., Andreis D., Girard J.F. (2017) *Electromagnetic methods in geophysics*, http://books.ifpenergiesnouvelles.fr/ebooks/ifpen-electro/.

Mayne W.H. (1962) Common reflection point horizontal data stacking techniques, *Geophysics* 27, 927-938, https://doi.org/10.1190/1.1439118.

Mendes M. (2009) A hybrid fast algorithm for first arrivals tomography, *Geophysical Prospecting* 57, 803-809, https://doi.org/10.1111/j.1365-2478.2008.00755.x.

Meunier J. (1998) Land 3D acquisition geometry: what is the cost of ground roll?, 68th annual international meeting, SEG, expanded abstracts, 58-61.

Meunier J. (1999) 3D geometry, velocity filtering and scattered noise, 69th annual international meeting, SEG, expanded abstracts, 1216-1219.

Meunier J. (2011) Seismic acquisition from Yesterday to Tomorrow, distinguished instructor series, n° 14, SEG, ISBN 978-1-56080-281-5 (volume), ISBN 978-1-56080-086-06 (series).

Meunier J., Gillot E. (2000) 3D seismic survey design: a solution, *First break* 18(5), 176-179.

Mikhael N. (2024) Investigating seismic velocity changes for an in-depth monitoring of the crustal mechanical properties in the Apennines, Italy, PhD, University Grenoble Alpes.

Mikhael N., Poli P., Garambois S. (2024) *Non-linear seismic velocity variations observed during a seismic swarm in the Alto Tiberina low angle normal fault from ambient noise correlation measurements*, JGR Solid Earth, https://doi.org/10.1029/2023JB028232.

Millouet J. (1961) Problèmes posés à la sismique dans la région parisienne, *Geophysical prospecting* IX(1), 1-18.

Miquelis F., Hanot F., Vicelli J., Kőrös M., Pöstyéni F. (2016) Geological modelling of static corrections for seismic processing, Example of Paris basin, France: New insight for onshore exploration, Petex.

Miquelis F., Hanot F., Vicelli J., Picornell V. (2019) Diagénèse de la Craie: application sismique, RST Caen.

Monk D., Yates M. (2000) 3D seismic survey design: a solution, *First break* 18(5), 180-183.

Mordret A., Shapiro N.M., Singh S., Roux P., Barkved O.I. (2013) Helmholtz Tomography of ambient noise surface wave data to estimate Scholte wave phase velocity at Valhall Life of the Field, *Geophysics* 78(2), WA99-WA109. https://doi.org/10.1190/geo2012-0303.1.

Morlier P., Sarda J.P. (1971) Atténuation des ondes élastiques dans les roches poreuses saturées, *Revue de l'Institut Français du Pétrole* 26(9), 731-755.

Mortensen J., Engstrom F., Lind I. (1998) The relation among porosity, permeability, and specific surface of chalk from the Gorm field, Danish North Sea, *SPE Reservoir Evaluation & Engineering* 1, 245-251.

Murphy C.A., Mumaw G.R. (2004) 3D Full Tensor Gradiometry: a high-resolution gravity measuring instrument resolving ambiguous geological interpretations, *ASEG Extended Abstracts* 1(1-4), https://doi.org/10.1071/ASEG2004ab104

Musser J.A. (2000) 3D seismic survey design: a solution, *First break* 18(5), 166- 171.

Nettleton L.L. (1939), Determination of density for the reduction of gravimeter observations, *Geophysics* 4, 176-183.

Nosjean N., Hanot F., Gruffeille J.P., Miquelis F., 2017, Statics: from imaging to interpretation pitfalls and an efficient way to overcome them, *First Break* 35(1), 175-188.

Palmer D. (1986) *Refraction seismic*, Geophysical Press, 13.

Pasaribu A.H., Pratama A.B., Machrani M. (2024) Evaluating Geothermal Fluid Production Impact on Density Using Time-Lapse Microgravity in Awibengkok Field, 5th Global Energy Transition Conference & Exhibition, Rotterdam, Nederland.

Pasquet S., Bodet L. (2017) SWIP: An integrated workflow for surface-wave dispersion inversion and profiling, *Geophysics* 82(6), WB47-WB61.

Piolat L., Geraud Y., Revil A., Diraison M., Favier A., Cosme P., 2024, Quantifying geophysical electrical signatures in hydrothermal reservoirs, 5th Global Energy Transition Conference & Exhibition, Rotterdam. Nederland

Quiblier J. (1997) *Propagation des ondes en géophysique et en géotechnique*, Modélisation par méthodes de Fourier, Editions Technip, Paris.

Reinsch T., et al. (2017) Utilizing supercritical geothermal systems: a review of past ventures and ongoing research activities, *Geothermal Energy* 5(1), 16.

Robein E. (2003) *Velocities, Time-Imaging and depth Imaging, in Reflection seismics*, Principles and Methods, EAGE Publications bv, ISBN 90-73781-28-0.

Roux P., Roueff A., Wathelet M. (2011) The San Andreas Fault revisited through seismic-noise and surface-wave tomography, *Geophys. Res. Lett*. 38, L13319.

Saade M., Robert S., Lempereur C., Grill M. (2024) Passive seismic tomography for 3D imaging of the subsurface in a tunnel area, Journees Scientifiques AGAP 2024, https://doi.org/10.1051/e3sconf/202450402001, EDP Sciences.

Shapiro N.M., Campillo M. (2004) Emergence of broadband Rayleigh waves from correlations of the ambient seismic noise, *Geophys. Res. Letters* 31, L07614, https://doi.org/10.1029/2004GL019491.

Shapiro N.M., Campillo M., Stehly L., Ritzwoller M. (2005) High Resolution Surface-Wave Tomography from Ambient Seismic Noise, *Science* 307, 1615-1618.

Souvannavong V., Aziez Y., Allo F., Rathore R., Stopin A., Bordenave A., Issautier B., Beccaletto L. (2024) Deep geothermal reservoir characterization with rock physics guided DNN, 5th Global Energy Transition Conference & Exhibition, Rotterdam, Nederland.

Vermeer G.J.O., Hornman K. (2000) Introduction to a 3D design problem, *First break* 18(5), 184-185.

Wyllie M.R.J., Gregory A.R., Gardner L.W. (1956) Elastic wave velocities in heterogeneous and porous media, *Geophysics* 21, 41-70.

Yang S., Wu G., Yang L., Zhang B., Jia Z. (2024) Velocity and temperature full waveform inversion from thermoacoustic equation based on L-S theory, 85th EAGE Annual Conference & Exhibition, Oslo, Norway.

Yilmaz O. (1987) Seismic data processing, SEG, Tulsa.